

Discovery of the Onset of Rapid Accretion by a Dormant Massive Black Hole.

D. N. Burrows¹, J. A. Kennea¹, G. Ghisellini², V. Mangano³, B. Zhang⁴, K. L. Page⁵, M. Eracleous¹, P. Romano³, T. Sakamoto^{6,7}, A. D. Falcone¹, J. P. Osborne⁵, S. Campana², A. P. Beardmore⁵, A. A. Breeveld⁸, M. M. Chester¹, R. Corbet^{6,7}, S. Covino², J. R. Cummings^{6,7}, P. D'Avanzo², V. D'Elia⁹, P. Esposito¹⁰, P. A. Evans⁵, D. Fugazza², J. M. Gelbord¹, K. Hiroi¹¹, S. T. Holland^{6,12}, K. Y. Huang¹³, M. Im¹⁴, G. Israel¹⁵, Y. Jeon¹⁴, Y.-B. Jeon¹⁶, N. Kawai^{17,20}, H. A. Krimm^{6,12}, P. Mészáros¹, H. Negoro¹⁸, N. Omodei¹⁹, W.-K. Park¹⁴, J. S. Perkins^{6,7}, M. Sugizaki²⁰, H.-I. Sung¹⁶, G. Tagliaferri², E. Troja^{21,22}, Y. Ueda¹¹, Y. Urata²³, R. Usui¹⁷, L. A. Antonelli^{15,9}, S. D. Barthelmy²¹, G. Cusumano³, P. Giommi⁹, F. E. Marshall²¹, A. Melandri², M. Perri⁹, J. L. Racusin²¹, B. Sbarufatti³, M. H. Siegel¹, & N. Gehrels²¹

April 4, 2019

Department of Astronomy & Astrophysics, The Pennsylvania State University, 525 Davey Laboratory, University Park, PA 16802, USA ²*INAF – Osservatorio Astronomico di Brera, Via Bianchi 46, 23807 Merate, Italy* ³*INAF – Istituto di Astrofisica Spaziale e Fisica Cosmica, Via U. La Malfa 153, I-90146 Palermo, Italy* ⁴*Department of Physics and Astronomy, University of Nevada, Las Vegas, NV 89154, USA* ⁵*Department of Physics and Astronomy, University of Leicester, University Road, LE1 7RH Leicester, UK* ⁶*CRESST and NASA/GSFC, Greenbelt, MD 20771, USA* ⁷*University of Maryland, Baltimore County, 1000 Hilltop Circle, Baltimore, MD 21250, USA* ⁸*University College London / Mullard Space Science Laboratory* ⁹*ASI Science Data Center, via Galileo Galilei, 00044 Frascati, Italy* ¹⁰*INAF – Osservatorio Astronomico di Cagliari, località Poggio dei Pini, strada 54, I-09012 Capoterra, Italy* ¹¹*Department of Astronomy, Kyoto University, Oiwake-cho, Sakyo-ku, Kyoto 606-8502, Japan* ¹²*Universities Space Research Association, 10211 Wincopin Circle, Suite 500, Columbia, MD 21044-3432, USA* ¹³*Academia Sinica Institute of Astronomy and Astrophysics, Taipei 106, Taiwan* ¹⁴*Center for the Exploration of the Origin of the Universe, Department of Physics & Astronomy, FPRD, Seoul National University, Shillim-dong, San 56-1, Kwanak-gu, Seoul, Republic of Korea* ¹⁵*INAF – Osservatorio Astronomico di Roma, via Frascati 33, I-00040 Monteporzio Catone, Italy* ¹⁶*Korea Astronomy and Space Science Institute (KASI), 776 Daedeokdae-ro, Yuseong-gu, Daejeon 305-348, Korea* ¹⁷*Department of Physics, Tokyo Institute of Technology, 2-12-1 Ookayama, Meguro-ku, Tokyo 152-8551, Japan* ¹⁸*Department of Physics, Nihon University, 1-8-14 Kanda-Surugadai, Chiyoda-ku, Tokyo 101-8308, Japan* ¹⁹*W. W. Hansen Experimental Physics Laboratory, Kavli Institute for Particle Astrophysics and Cosmology, Department of Physics and SLAC National Accelerator Laboratory, Stanford University, Stanford, CA 94305, USA* ²⁰*MAXI team, RIKEN, 2-1 Hirosawa, Wako, Saitama 351-0198* ²¹*NASA Goddard Space Flight Center, Greenbelt, MD 20771, USA* ²²*Oak Ridge Associated Universities* ²³*Institute of Astronomy, National Central University, Chung-Li 32054, Taiwan*

Massive black holes are believed to reside at the centres of most galaxies. They can become detectable by accretion of matter, either continuously from a large gas reservoir or impulsively from the tidal disruption of a passing star, and conversion of the gravitational energy of the infalling matter to light. Continuous accretion drives Active Galactic Nuclei (AGN), which are known to be variable but have never been observed to turn on or off. Tidal disruption of stars by dormant massive black holes has been inferred indirectly but the onset of a tidal disruption event has never been observed. Here we report the first discovery of the onset of a relativistic accretion-powered jet in the new extra-

galactic transient, Swift J164449.3+573451. The behaviour of this new source differs from both theoretical models of tidal disruption events and observations of the jet-dominated AGN known as blazars. These differences may stem from transient effects associated with the onset of a powerful jet. Such an event in the massive black hole at the centre of our Milky Way galaxy could strongly ionize the upper atmosphere of the Earth, if beamed towards us.

Swift J164449.3+573451 (hereafter Sw J1644+57) was discovered by the *Swift*¹ Burst Alert Telescope² (BAT, 15-150 keV) in a 20-minute image of the sky that began at 12:57:45 UT on 28 March 2011³. The *Swift* X-Ray Telescope⁴ (XRT) began observing the field at 13:22:19.8 UT and found a bright, uncatalogued X-ray source. The most accurate XRT position^{5,6} is RA (J2000): $16^{\text{h}} 44^{\text{m}} 49.92^{\text{s}}$, Dec (J2000): $+57^{\circ} 35' 00.6''$, with a 90% confidence error circle radius of 1.4 arcseconds. A precise localization by the EVLA found a variable source at the centre of a galaxy within the XRT error circle⁷. Optical spectroscopy of this source^{8,9} measured a redshift of 0.354, corresponding to a luminosity distance¹ of 5.8×10^{27} cm.

Subsequent analysis of BAT data taken before the on-board trigger shows that the outburst was first detected on 25 March 2011, with peak BAT count rates of $\sim 0.02 \text{ cts cm}^{-2} \text{ s}^{-1}$ during the days just before the on-board trigger (Supplementary Figure 1)². Beginning on 28 March the BAT data show multiple flares peaking at up to $0.09 \text{ cts cm}^{-2} \text{ s}^{-1}$ (about 20% of the count rate from the Crab nebula). The source flux then dropped dramatically, with an average count rate of $0.0020 \pm 0.0005 \text{ cts cm}^{-2} \text{ s}^{-1}$ between 2 April 2011 and 18 April 2011.

The flares seen by BAT are tracked in the 0.3-10 keV band by the XRT (Figure 1, Supplementary Figures 1 and 2). Following nearly 3 days of intense flaring with peak fluxes³ over $5 \times 10^{-9} \text{ erg cm}^{-2} \text{ s}^{-1}$, Sw J1644+57 decayed over several days to a flux of about $8 \times 10^{-12} \text{ erg cm}^{-2} \text{ s}^{-1}$, then rose rapidly to $\sim 8 \times 10^{-10} \text{ erg cm}^{-2} \text{ s}^{-1}$ (Figure 2). Over the next two weeks the X-ray flux decayed gradually to $\sim 1.5 \times 10^{-10} \text{ erg cm}^{-2} \text{ s}^{-1}$,

¹assuming $H_0 = 71 \text{ km s}^{-1}$, $\Omega_m = 0.27$, and $\Omega_\Lambda = 0.73$.

²During the brightest parts of the outburst, Sw J1644+57 had power law photon indices ranging from 1.3 to 1.8 in the BAT bandpass; the corresponding flux conversion factor is $\sim 10^{-7} \text{ erg/count}$. See Supplementary Table 1.

³All XRT fluxes are for the 0.3-10 keV band.

with occasional sharp dips to $\lesssim 3 \times 10^{-11}$ erg cm $^{-2}$ s $^{-1}$. No statistically significant periodic or quasi-periodic signals were found in the XRT data (see Supplementary Methods).

The X-ray spectral shape varies strongly with X-ray flux in the first few days after the BAT trigger (Supplementary Figures 3 and 4). A simple power law can fit the spectra, but the fits are improved with one of several more complex models (see Supplementary Methods for details). Substantial absorption in the host galaxy is required, with $N_{\text{H}} \sim 2 \times 10^{22}$ cm $^{-2}$ (Supplementary Figure 5).

We obtained photometry in the uvw2, uvm2, uvw1, u, b, v, R, J, H, and Ks bands, as well as broad-band “white” with the *Swift* UVOT, TNG, BOAO, LOAO, and Maidanak Observatory telescopes (see Supplementary Methods for details). The heavily obscured optical counterpart of the transient X-ray source is not detected in optical or UV bands, where the host galaxy dominates the light, but is detected strongly in the near-infrared.

Upper limits from the *Fermi* Large Area Telescope¹⁰ (LAT) and from *VERITAS*¹¹ provide constraints in the GeV and TeV band, respectively (see Supplementary Methods for details).

Archival X-ray and γ -ray data show no evidence of Sw J1644+57 before 25 March 2011. X-ray flux upper limits from observations between 1990 and March 24 are orders of magnitude lower than the peak X-ray fluxes observed by BAT and XRT, and are significantly lower than the lowest flux recorded by XRT since *Swift* observations began on 28 March 2011 (see details in Supplementary Methods). The source has brightened by at least 4 orders of magnitude compared with some earlier deep observations of this field, and we consider that the source was truly dormant for decades before this outburst began.

The abrupt appearance of a bright new persistent extragalactic X-ray source is unprecedented. Gamma-ray bursts reach similar fluxes, but fade rapidly much more rapidly than Sw J1644+57. Blazars (AGN with energetic jets pointed toward Earth) are known to be highly variable, but are persistent and have never been observed to turn off or to turn on, or display this level of variability. Supernovae in distant galaxies are rarely detected at X-ray wavelengths.

The isotropic X-ray luminosity⁴ of Sw J1644+57 (corrected for absorption in the source) ranges from $10^{45} - 4 \times 10^{48}$ erg s $^{-1}$, with an integrated X-ray power⁴ (over the 23 days following the BAT trigger) of $\sim 3 \times 10^{53}$ erg. If Sw J1644+57 radiates isotropically, its total energy production is significantly larger than the electromagnetic energy released by a supernova explosion. The persistence of the X-ray emission implies that this object is not powered by an impulsive event such as an exploding star; instead, it requires a continuous production of prodigious amounts of energy. Only gravitational energy released by accretion of matter in the vicinity of a black hole can produce such power levels over such a long time period.

The observed minimum 3σ X-ray variability time scale of Sw J1644+57, $\delta t_{\text{obs}} \sim 100$ s, constrains the size of the black hole under the assumption that the central engine dominates the variability⁵. For a Schwarzschild black hole with mass M_{bh} and radius r_s , the minimum variability time scale in its rest frame is $\delta t_{\text{min}} \sim r_s/c \sim 10.0(M_6)$ s, where $M_6 = (M_{\text{bh}}/10^6 M_{\odot})$. At $z = 0.354$, this gives

$$M_{\text{bh}} \sim 7.4 \times 10^6 \left(\frac{\delta t_{\text{obs}}}{100 \text{ s}} \right) M_{\odot}. \quad (1)$$

Much smaller masses are unlikely. The black hole mass can also be constrained through the $M_{\text{bh}} - L_{\text{bulge}}$ relation, which gives an upper limit of $2 \times 10^7 M_{\odot}$. We conclude that the black hole mass is in the range $1 < M_6 < 20$ (see Supplementary Discussion).

The Eddington luminosity⁶ of this black hole is $L_{\text{Edd}} = 1.3 \times 10^{44}$ erg s $^{-1} M_6$. The observed peak luminosity is super-Eddington

and requires a strongly anisotropic radiation pattern with a relativistic jet pointed towards us. A relativistic jet is also required by the radio transient⁷, which we interpret as an external shock in the gas surrounding Sw J1644+57.

The spectral energy distribution (SED) produced from our data (Figure 3) shows that the broad-band energy spectrum is dominated by the X-ray band, which accounts for 20% (50%) of the total bolometric energy output in the low (high/flaring) X-ray state⁴. The SED places strong constraints on the emission mechanism. The IR-to-X-ray slope, nearly as hard as $\nu^{1/3}$, can only be accommodated within synchrotron theory in the absence of low-energy electrons, which would severely overproduce the optical flux. This requires a particle-starved source, implying that the jet is magnetically-dominated (see Supplementary Discussion for details, and discussion of other models). At high energies, the upper limits from *Fermi* and *VERITAS* require that the self-Compton flux from the X-ray peak is absorbed by the $\gamma\gamma \rightarrow e^{\pm}$ process. The bulk Lorentz factor in the X-ray emitting region must therefore be $\Gamma \lesssim 20$; we assume a value of ~ 10 .

This luminous, accretion-powered, relativistic jet can be powered by the tidal disruption of a star or by the onset of AGN activity from a previously dormant massive black hole. The *Swift* BAT, with a field of view of $\sim 4\pi/7$ sr, has detected one such event in ~ 7 years at a flux that would have been detectable to $z \sim 0.8$. The all-sky rate of Sw J1644+57-like events is therefore $R_{4\pi} \sim 1 \text{ yr}^{-1}$, with a 90% confidence interval¹² of $0.08 - 3.9 \text{ yr}^{-1}$. The rate of tidal disruption events is thought to be $\sim 10^{-5} \text{ yr}^{-1} \text{ galaxy}^{-1}$ on both observational¹³ and theoretical¹⁴ grounds. Given the galaxy number density $n_{\text{gal}} \sim 0.01 \text{ Mpc}^{-3}$, the total number of galaxies in the co-moving volume within $z < 0.8$ can be estimated as $N_{\text{gal}}(z < 0.8) \sim 10^9$. This gives a total tidal disruption event rate of $R_{\text{TD},4\pi}(z < 0.8) \sim 10^4 \text{ yr}^{-1}$. If these act like AGN, 10% of them contain relativistic (“radio-loud”) jets. The fraction of these jets that point towards us is

$$\max \left(\frac{1}{2\Gamma^2}, \frac{\theta_j^2}{2} \right),$$

where Γ is the bulk Lorentz factor and θ_j is the opening angle of the jet. A bulk Lorentz factor of $\Gamma \sim 10 - 20$ or a jet opening angle of $\theta_j \sim 5^\circ$ would provide the observed event rate. Our observations are consistent with theoretical predictions of the formation of a low-density, magnetically-dominated jet during the super-Eddington phase of a tidal disruption event around a $10^6 - 10^7 M_{\odot}$ black hole¹⁵. In the tidal disruption interpretation, we expect the source to begin a slow decay once the material in the accretion disk is exhausted and the luminosity begins to track the fall-back timescale ($t^{-5/3}$) of the disrupted stellar material onto the black hole¹⁶. This decay may have begun a few days after the BAT trigger (Figure 2).

A dormant massive black hole could also become visible through the onset of long-lived AGN activity. The typical life time of an AGN is $t_{\text{AGN}} \sim 3 \times 10^7 \text{ yr}$ ¹⁷. In steady-state, the rate at which AGN turn on is therefore $\sim t_{\text{AGN}}^{-1}$ (but see Supplementary Discussion). Within the $z < 0.8$ volume, the event rate of the onset of a new radio-loud AGN would be $R_{\text{AGN,tot}} = 0.1 N_{\text{gal}}(z < 0.8) / t_{\text{AGN}} \sim 3 \text{ yr}^{-1}$. A moderate Lorentz factor of $\Gamma \sim 3$ or an opening angle of $\theta_j \sim 13^\circ$ would have an event rate of $\sim 0.1 \text{ yr}^{-1}$, consistent with the observations. The onset could be initiated by an accretion disk in a rotating galactic bulge, populated by gravitationally captured mass lost from stars in the inner galaxy through supernovae or stellar winds. The inner radius of this disk will decrease slowly under the effect of α viscosity, with a final infall timescale of $t_d \sim 2 \times 10^3 (\alpha/0.1)^{-1} M_6$ s, resulting in a rapid onset of electromagnetic radiation. In this case one expects an extremely long-lived event ($\sim t_{\text{AGN}}$). Long-term monitoring of Sw J1644+57 will be required to distinguish between these scenarios for the accretion.

We can consider Sw J1644+57 to be an analog of Sgr A*, the massive black hole in the centre of our Milky Way galaxy. Sgr A* has a mass of $\sim 4 \times 10^6 M_{\odot}$ ^{18,19}, and yet has a quiescent soft X-ray luminosity^{20,21} of

⁴In the XRT band, which is 0.4–13.5 keV in the Sw J1644+57 rest frame.

⁵Variability can also be produced in the jet, as is seen in blazars..

⁶The luminosity at which the gravitational force on infalling gas is balanced by outward radiation pressure.

only 4×10^{32} erg s $^{-1}$, which would be undetectable at $z=0.354$. If a jet similar to Sw J1644+57 turned on in Sgr A* and was pointed at Earth, the peak X-ray flux at the Earth could reach ~ 200 erg cm $^{-2}$ s $^{-1}$. The X-ray flux would correspond to a Y200-class solar flare, >40 times brighter than the strongest X-ray flare ever detected from the Sun²², and the fluence (integrated flux) could exceed 10^4 J m $^{-2}$. Such an event would produce strong ionization effects on the Earth's atmosphere, and the total fluence is $>10\%$ of that thought necessary to produce mass extinctions in the case of a 10 s duration γ -ray burst²³. Fortunately, the probability of a Sgr A* jet being pointed at Earth is low.

References

1. Gehrels, N. *et al.* The Swift Gamma-Ray Burst Mission. *Ap. J.* **611**, 1005–1020 (2004).
2. Barthelmy, S. D. *et al.* The Burst Alert Telescope (BAT) on the SWIFT Midex Mission. *Space Sci. Rev.* **120**, 143–164 (2005). [arXiv:astro-ph/0507410](https://arxiv.org/abs/astro-ph/0507410).
3. Cummings, J. R. *et al.* GRB 110328A: Swift detection of a burst. *GRB Coordinates Network, Circular Service* **11823** (2011).
4. Burrows, D. N. *et al.* The Swift X-Ray Telescope. *Space Sci. Rev.* **120**, 165–195 (2005). [arXiv:astro-ph/0508071](https://arxiv.org/abs/astro-ph/0508071).
5. Goad, M. R. *et al.* Accurate early positions for Swift GRBs: enhancing X-ray positions with UVOT astrometry. *Astron. and Astrophys.* **476**, 1401–1409 (2007). 0708.0986.
6. Evans, P. A. *et al.* Methods and results of an automatic analysis of a complete sample of Swift-XRT observations of GRBs. *MNRAS* **397**, 1177–1201 (2009). 0812.3662.
7. Zauderer, A. *et al.* The Birth of a Relativistic Outflow in the Unusual γ -ray Transient Swift J164449.3+573451. *Nature*, submitted (2011).
8. Levan, A. J., Tanvir, N. R., Wiersema, K. & Perley, D. GRB 110328A: Gemini spectroscopic observations. *GRB Coordinates Network, Circular Service* **11833** (2011).
9. Thoene, C. C. *et al.* GRB 110328A / Swift J164449.3+573451: optical spectroscopy from GTC. *GRB Coordinates Network, Circular Service* **11834** (2011).
10. Atwood, W. B. *et al.* The Large Area Telescope on the Fermi Gamma-Ray Space Telescope Mission. *Ap. J.* **697**, 1071–1102 (2009). 0902.1089.
11. Aliu, E. *et al.* The VERITAS Collaboration. *in prep.* (2011).
12. Kraft, R. P., Burrows, D. N. & Nousek, J. A. Determination of confidence limits for experiments with low numbers of counts. *Ap. J.* **374**, 344–355 (1991).
13. Gezari, S. *et al.* Luminous Thermal Flares from Quiescent Supermassive Black Holes. *Ap. J.* **698**, 1367–1379 (2009). 0904.1596.
14. Wang, J. & Merritt, D. Revised Rates of Stellar Disruption in Galactic Nuclei. *Ap. J.* **600**, 149–161 (2004). [arXiv:astro-ph/0305493](https://arxiv.org/abs/astro-ph/0305493).
15. Strubbe, L. E. & Quataert, E. Optical flares from the tidal disruption of stars by massive black holes. *MNRAS* **400**, 2070–2084 (2009). 0905.3735.
16. Lodato, G., King, A. R. & Pringle, J. E. Stellar disruption by a supermassive black hole: is the light curve really proportional to $t^{-5/3}$? *MNRAS* **392**, 332–340 (2009). 0810.1288.
17. Krolik, J. H. *Active galactic nuclei : from the central black hole to the galactic environment* (Princeton University Press, 1999).
18. Ghez, A. M. *et al.* Measuring Distance and Properties of the Milky Way's Central Supermassive Black Hole with Stellar Orbits. *Ap. J.* **689**, 1044–1062 (2008). 0808.2870.
19. Gillessen, S. *et al.* Monitoring Stellar Orbits Around the Massive Black Hole in the Galactic Center. *Ap. J.* **692**, 1075–1109 (2009). 0810.4674.
20. Baganoff, F. K. *et al.* Rapid X-ray flaring from the direction of the supermassive black hole at the Galactic Centre. *Nature* **413**, 45–48 (2001). [arXiv:astro-ph/0109367](https://arxiv.org/abs/astro-ph/0109367).
21. Shcherbakov, R. V. & Baganoff, F. K. Inflow-Outflow Model with Conduction and Self-consistent Feeding for Sgr A*. *Ap. J.* **716**, 504–509 (2010). 1004.0702.
22. Thomson, N. R., Rodger, C. J. & Clilverd, M. A. Large solar flares and their ionospheric D region enhancements. *Journal of Geophysical Research (Space Physics)* **110**, A06306 (2005).
23. Thomas, B. C. *et al.* Terrestrial Ozone Depletion due to a Milky Way Gamma-Ray Burst. *Ap. J. (Letters)* **622**, L153–L156 (2005). [arXiv:astro-ph/0411284](https://arxiv.org/abs/astro-ph/0411284).
24. Ghisellini, G. & Tavecchio, F. Canonical high-power blazars. *MNRAS* **397**, 985–1002 (2009). 0902.0793.

Supplementary Information is linked to the online version of the paper at www.nature.com/nature.

Acknowledgements DNB, JAK, and JMG acknowledge support by NASA contract NAS5-00136. JPO, KLP, PAE, and APB acknowledge the support of the UK Space Agency. We thank Dr. Andrew Read for help with the most recent XMM slew data. SCA, SCo, PD'A, DF, GT, LAA,

GC, AM, and BS acknowledge financial support from the agreement ASI-INAF I/004/11/0. VM and PR acknowledge financial contribution from the agreement ASI-INAF I/009/10/0. PE acknowledges financial support from the Autonomous Region of Sardinia under the program PO Sardegna FSE 2007–2013, L.R. 7/2007. BZ acknowledges NSF (AST-0908362) and NASA (NNX10AD48G) for support. ET was supported by an appointment to the NASA Postdoctoral Program at the Goddard Space Flight Center, administered by Oak Ridge Associated Universities through a contract with NASA. NK acknowledges support by the Ministry of Education, Culture, Sports, Science and Technology (MEXT) through Grant-in-Aid for Science Research 19047001. KH, NK, HN, MS, YUe, and RU thank the MAXI operation team. MI, WK, and YJ acknowledge support from the CRI grant 2009-0063616, funded by the Korean government (MEST). KYH and YU acknowledge support from the NSC grants 99-2112-M-002-002-MY3 and 98-2112-M-008-003-MY3. The *Fermi* LAT Collaboration acknowledges support from a number of agencies and institutes for both development and the operation of the LAT as well as scientific data analysis. These include NASA and DOE in the United States, CEA/Irfu and IN2P3/CNRS in France, ASI and INFN in Italy, MEXT, KEK, and JAXA in Japan, and the K. A. Wallenberg Foundation, the Swedish Research Council and the National Space Board in Sweden. Additional support from INAF in Italy and CNES in France for science analysis during the operations phase is also gratefully acknowledged. We acknowledge the use of public data from the *Swift* data archive. This work also made use of data supplied by the UK Swift Science Data Centre at the University of Leicester. The Fermi data are available from <http://fermi.gsfc.nasa.gov/ssc/>. We gratefully acknowledge the contribution of pre-publication upper limits by the *VERITAS* Collaboration.

Author Contributions DNB, JAK, and ME composed the text, based on inputs from the other co-authors. Theoretical interpretation was provided by GG, BZ, ME, and PM, with contributions by ADF and SC. JAK, VM, KLP, JPO, PR, SCA, APB, VD'E, PE, PAE, and GI processed and analyzed the *Swift* XRT data. TS, JRC, and HAK processed and analyzed the *Swift* BAT data. Optical/NIR data were obtained with the TNG, BOAO, and LOAO telescopes and were provided, reduced, and analyzed by SCo, PD'A, DF, KYH, MI, YJ, Y-BJ, W-KP, H-IS, GT, YUe, and LAA. *Swift* UVOT data were processed and analyzed by AAB, MMC, and STH with contributions by FEM. *Fermi* LAT data analysis was performed by RC, NO, JSP, and ET. KH, NK, HN, MS, YUe, and RU processed and analyzed the MAXI data. ADF provided liaison with the *VERITAS* Collaboration. JG and PG provided analysis of ROSAT archival data, and JO provided analysis of archival XMM data. All authors discussed the results and commented on the manuscript.

Author Information *Swift* data are available from the NASA HEASARC (<http://swift.gsfc.nasa.gov/docs/swift/archive/>) or from mirror sites in the UK (http://www.swift.ac.uk/swift_portal/archive.php) and Italy (<http://swift.asdc.asi.it/>). Reprints and permissions information is available at www.nature.com/reprints. The authors have no competing financial interests. Correspondence should be addressed to DNB (burrows@astro.psu.edu).

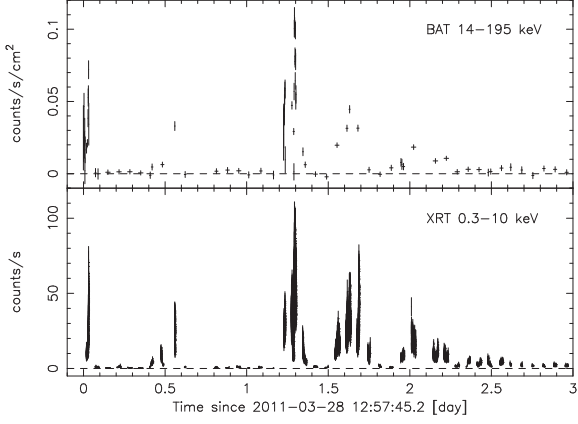


Figure 1 | Swift BAT (top) and XRT (bottom) light curves of the early flares from Sw J1644+57. The horizontal axis is time since the BAT trigger on 28 March 2011. The BAT and XRT count rates track each other, with episodes of flaring in the first few days after the BAT trigger on 28 March 2011. Data gaps are caused by times when the source was not being observed. Error bars are one standard deviation.

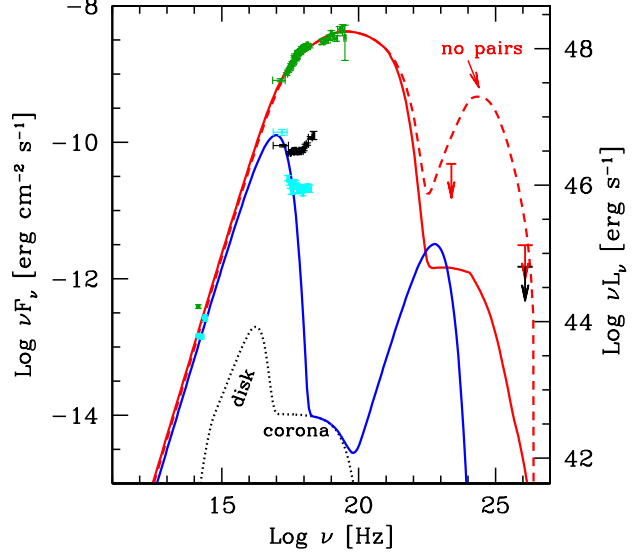


Figure 3 | The Spectral Energy Distribution (SED) of Sw J1644+57. The green data points show the transient brightness a few days after the BAT trigger; cyan data points show the measured SED at 4.5 days; black data points are XRT data between 6.5 and 9.5 days after the BAT trigger. Near-infrared (NIR) were obtained with the TNG and BOAO telescopes in the Ks band 48 hours after the trigger, and in the J, H, and Ks band fluxes 4.5 days after trigger. The NIR flux has been dereddened with $A_V = 4.5$. Details of the observations and data reduction are presented in Supplementary Methods. In the X-ray band we show the spectrum at the peak of the bright flares (31 hours after BAT trigger; XRT and BAT) and in the low flux state (~ 4.5 days after, XRT only), together with the spectrum in the intermediate persistent flux state that began a week after the BAT trigger (time integrated between day 6.5 and 9.5 from trigger, XRT only). The X-ray data have been corrected for absorption with a constant $N_H = 2 \times 10^{22} \text{ cm}^{-2}$. Upper limits from the *Fermi* LAT at $2 \times 10^{23} \text{ Hz}$ and from *VERITAS*¹¹ at 10^{26} Hz are also shown. The red curve shows the model discussed in the text, which is a blazar jet model²⁴ fit to our SED. The dominant emission mechanism is synchrotron radiation peaking in the X-ray band. On the low frequency side, the hard slope between the NIR and X-ray bands requires suppression of low-energy electrons, which would otherwise overproduce the NIR flux. On the high frequency side, the LAT and *VERITAS* upper limits require that the self-Compton component is suppressed by $\gamma\gamma$ pair production. The model includes a disk/corona component from the accretion disk (black dotted curve), but the flux is dominated at all frequencies by the synchrotron component from the jet. The blue curve shows the corresponding model in the low X-ray flux state. The kink in the X-ray spectrum suggests that a possible additional component may be required; it would have to be very narrow, and its origin is unclear. The model parameters for this fit are given in the Supplementary Discussion, and suggest a magnetically-dominated jet, which is unusual for AGN. This might be explained by the unusually high accretion rate and small black hole mass (compared to typical AGN) implied by our data. In the SI we discuss two alternative models: one with a magnetically-dominated jet but a more AGN-like parameter set, and one at the opposite extreme of a particle-dominated jet. Both of these alternative models seem contrived, and we favor the model presented here. All error bars are one standard deviation.

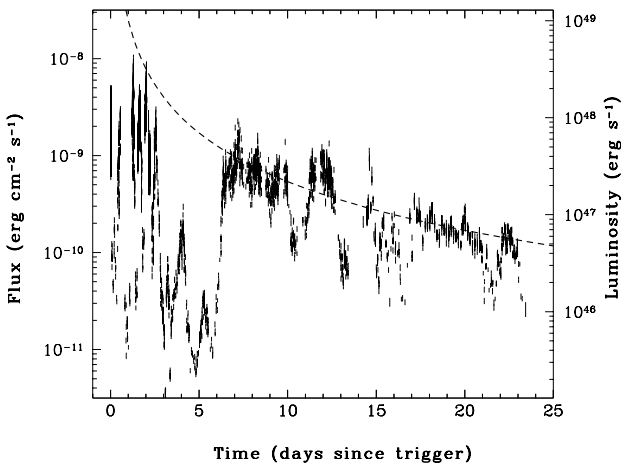


Figure 2 | Swift XRT light curve of Sw J1644+57 for the first 3 weeks of observations. The X-ray events were summed into time bins containing 200 counts per bin and count rates were calculated for each time bin. Because of the strong spectral evolution of this source and its large intrinsic absorption, light curves in physical units cannot be produced with constant count rate-to-flux conversion factors. We use time-dependent conversion factors to convert count rates to fluxes. Spectral fits were performed on time slices of data that typically contained about 3000 counts (see Supplementary Methods). Count rate-to-flux conversion factors were calculated for each spectrum, using absorption-corrected fluxes in the rest frame 0.4–13.5 keV band. These time-dependent flux conversion factors were then interpolated to obtain fluxes for each time bin. The right-hand axis gives the conversion to luminosity of the source, assuming isotropic radiation. The dashed line shows a $t^{-5/3}$ curve (where t is time since the BAT trigger). Error bars are one standard deviation.

Discovery of the Onset of Rapid Accretion by a Dormant Massive Black Hole: Supplementary Information

Supplementary Methods

Swift Discovery and broad-band observations

BAT data The *Swift*²⁵ Burst Alert Telescope²⁶ (BAT, 15–150 keV) triggered on a new uncatalogued source at $T_0 = 12:57:45$ UT 28 March 2011²⁷. The trigger was assumed to be a γ -ray burst (GRB) and was named GRB 110328A, following standard nomenclature. However, this trigger was followed by three additional BAT triggers at increasing count rates over the next two days²⁸ (see Supplementary Table 1), making it clear that this object was not, in fact, a GRB. (Following the fourth trigger, the on-board BAT source catalog was adjusted to prevent further triggers.) The X-ray counterpart was renamed Swift J164449.3+573451, which is now the preferred name of the source²⁹. We will refer to Swift J164449.3+573451 as Sw J1644+57 for the remainder of this paper.

Post-facto examination of pre-trigger data indicate that the outburst was first detected by BAT on 25 March 2011 with a mean count rate (integrated over 24 hours) of (0.0059 ± 0.0016) cts $\text{cm}^{-2} \text{s}^{-1}$ (too low to generate an on-board trigger). We note that the source was outside the BAT FOV for 2.86 hours before the first trigger. Between 25 March and 31 March the BAT data show multiple flares peaking at up to 0.09 cts $\text{cm}^{-2} \text{s}^{-1}$ (about 22 mCrabs). During the brightest parts of the outburst, the source had power law photon indices ranging from 1.3 to 1.8. The average 15–150 keV flux in the time interval 12:57:45 UT on 28 March 2011 to 05:30 UT on 30 March 2011 was about $(1.0 \pm 0.2) \times 10^{-9}$ erg $\text{cm}^{-2} \text{s}^{-1}$. The source flux then dropped dramatically, with an average count rate of 0.002 ± 0.0005 cts $\text{cm}^{-2} \text{s}^{-1}$ between 2 April 2011 and 12 April 2011 (see Supplementary Figure 1).

For most of the BAT data the spectral slope cannot be determined, making it difficult to determine an accurate flux based on the count rates. However if we assume a spectral slope, we can obtain estimates of the 15–150 keV flux. Supplementary Table 2 provides flux conversion factors for average BAT count rates at 3 epochs, for 2 observed spectral slopes.

XRT data Observations of Sw J1644+57 with the *Swift* X-ray Telescope³⁰ (XRT, 0.3–10 keV) began at 13:20:52 UT on 28 March 2011. XRT observed Sw J1644+57 daily for between 11 ks and 28 ks per day. We report here on the first 23 days after the trigger, during which the mean time spent on-target was 15.2 ks per day. As *Swift* is in a low-Earth orbit, observations are broken into small snapshots, typically 20–30 min long per ~ 96 min *Swift* orbit.

For the first 14.5 days the XRT was in “Auto State”, in which it autonomously selects the appropriate observing mode based upon the brightness of the observed source. This meant that as the source varied in brightness, the XRT collected data in a combination of Windowed Timing (WT) and Photon Counting (PC) modes. PC mode is the standard

Supplementary Table 1 | *Swift* BAT trigger details for Sw J1644+57.

Trigger Number	Date	Time UT	Trigger Duration (s)	Intensity (counts s^{-1})
450158	28 Mar	12:57:45	1208	6.1
450161	28 Mar	13:40:41	64	19.4
Threshold set to 0 so BAT would trigger on it again				
450257	29 Mar	18:26:25	320	15.6
450258	29 Mar	19:57:45	64	38.2
Triggers from this source disabled				

Supplementary Table 2 | Flux conversion for observed BAT count rates for different spectral slopes

Time Period	BAT count rate (cts s ⁻¹ cm ⁻²)	Photon Index (assumed)	Estimated Flux (erg cm ⁻² s ⁻¹ , 15-150 keV)
Pre-Trigger	0.0059	1.8	5.1×10^{-10}
	0.0059	1.3	6.1×10^{-10}
Peak rate	0.0900	1.8	7.8×10^{-9}
	0.0900	1.3	9.3×10^{-9}
Late time	0.0020	1.8	1.7×10^{-10}
	0.0020	1.3	2.1×10^{-10}

Supplementary Table 3 | *Swift* UVOT UV upper limits.

Filter	$T_0 + 0 - 2$ days		$T_0 + 2 - 15$ days	
	Exposure (s)	UL (3 σ)	Exposure (s)	UL (3 σ)
white	18359	>23.6	11221	>23.5
v	2541	>21.1	<i>no observations</i>	
b	1493	>21.5	<i>no observations</i>	
u	31593	>23.1	37032	>23.2
w1	3422	>21.8	82742	>23.5
m2	3048	>21.6	38324	>23.1
w2	2320	>21.8	24763	>23.1

XRT imaging mode, with a timing resolution of 2.5 s; if a source is brighter than ~ 0.5 XRT count s⁻¹ in this mode, pile-up correction must be used³¹. WT mode is a fast timing mode (1.8 ms time resolution) that collects 1-dimensional image data. The fast readout of WT mode means that pile-up is avoided for sources with a count rate below ~ 100 counts s⁻¹.

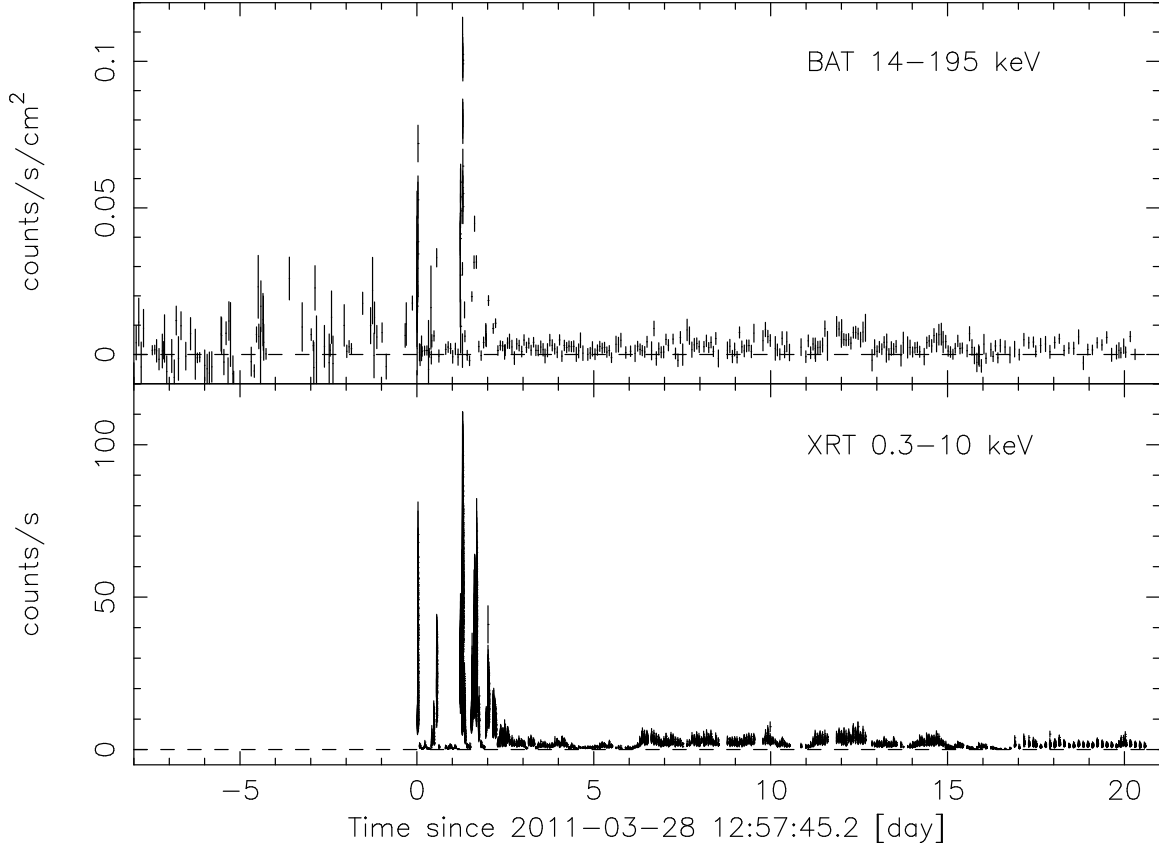
The switch points for Auto State are tuned specifically for GRB observations, i.e. a fading X-ray light curve. For sources of moderate brightness (1-5 XRT counts s⁻¹), data will often be collected in PC mode. For this reason we changed our observing mode to WT for data collected from 12 April 2011 onwards, to avoid issues relating to pile-up.

X-ray spectra and light curves were produced utilizing the methods described by Evans et al.³² All PC mode data were corrected for pile-up by removing events from the core of the PSF, and utilizing the wings of the PSF for both spectral fitting and light curve generation³¹. XRT spectra were corrected for the effects of charge traps that have developed due to radiation damage to the CCD over the *Swift* mission lifetime.

The XRT count rate light curve for Sw J1644+57 is shown in Supplementary Figure 2. Total exposure time for the first 23.4 days is 3.56×10^5 s, with a live time fraction of 17.6%.

We produced light curves in two energy bands (soft and hard) in order to examine spectral variations with time and flux. We observe a strong anti-correlation in WT mode data between the spectral hardness and flux, with softer spectra as the source intensity decreases (see Supplementary Figure 3). There is a similar correlation in PC mode data, but the scatter is larger and the correlation is weaker.

UVOT data The *Swift* UV-Optical Telescope³³ (UVOT) observed Sw J1644+57 in all optical and ultraviolet filters immediately following each of the four *Swift* BAT triggers, switching to mainly the ultraviolet filters for deep imaging after 1 April 2011. Observing periods were the same as for XRT. No persistent source has been detected in any filter. Photometry has been performed on individual and summed images using the UVOT photometric system³⁴. No correction has been applied for Galactic extinction due to the reddening of $E_{B-V} = 0.024$ in the direction of the transient³⁵. Supplementary Table 3 provides the upper limits for two epochs: early X-ray variability (first two days after the *Swift* BAT trigger), and later times.



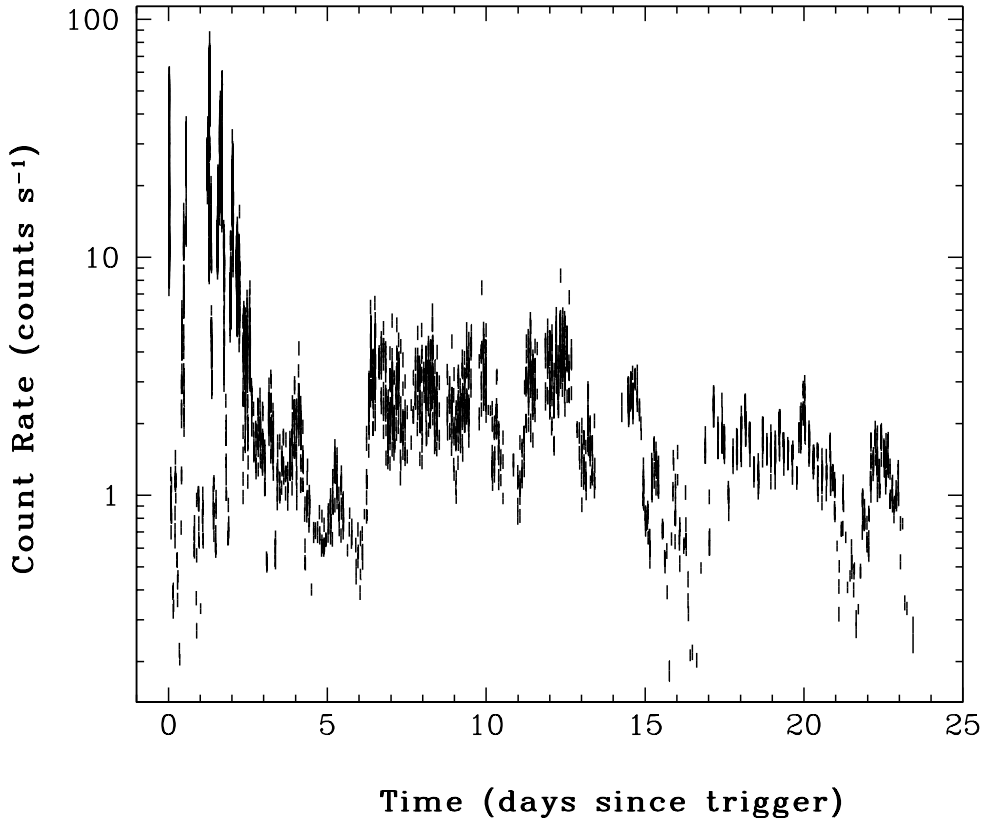
Supplementary Figure 1 | BAT (top) and XRT (bottom) light curves of Sw J1644+57. Times are measured from the BAT trigger on 28 March 2011. Although the higher count rate in the XRT allows better time resolution, it is clear that the count rates in both instruments track each other, with numerous flares in the first few days after the BAT trigger. Note that Sw J1644+57 was detected by BAT \sim 4–5 days before BAT triggered and XRT observations began. Data gaps are caused by periods when the source was not being observed.

XRT Timing analysis

After applying the barycentric correction to the XRT event lists we searched for coherent or quasi-periodic signals over different energy ranges and time intervals by using Fourier techniques. Due to the presence of strong non-Poissonian noise, mainly introduced by the rapid variability of the source, particular care must be taken in evaluating the statistical significance of any candidate signal. Following the prescriptions of Israel & Stella³⁶, no significant (periodic or quasi-periodic) signal was found. Conservative 3σ upper limits on the pulsed fraction, defined as semi-amplitude of the sinusoid divided by the mean source count rate, were computed. For the data span in the 31 March 2011 to 19 April 2011 interval (i.e. without the initial intense spikes in order to mitigate the low frequency noise in the power spectrum) and the energy range 0.3 – 10 keV (524288 trials between 1×10^{-6} and 0.2 Hz), the 3σ upper limits are in the 1%-3% range for periods shorter than 500s, and in the 5%-90% range for periods between \sim 500s and 1000s.

X-ray spectral analysis

The XRT data were processed with standard procedures (XRTPipeline v0.12.4), filtering and screening criteria by using FTOOLS in the HEASOFT package (v.6.9). We used the latest (pre-release) version of the XRT software task *xrtcalcpi*, which calculates Pulse Invariant (PI) event energies taking into account position dependent corrections



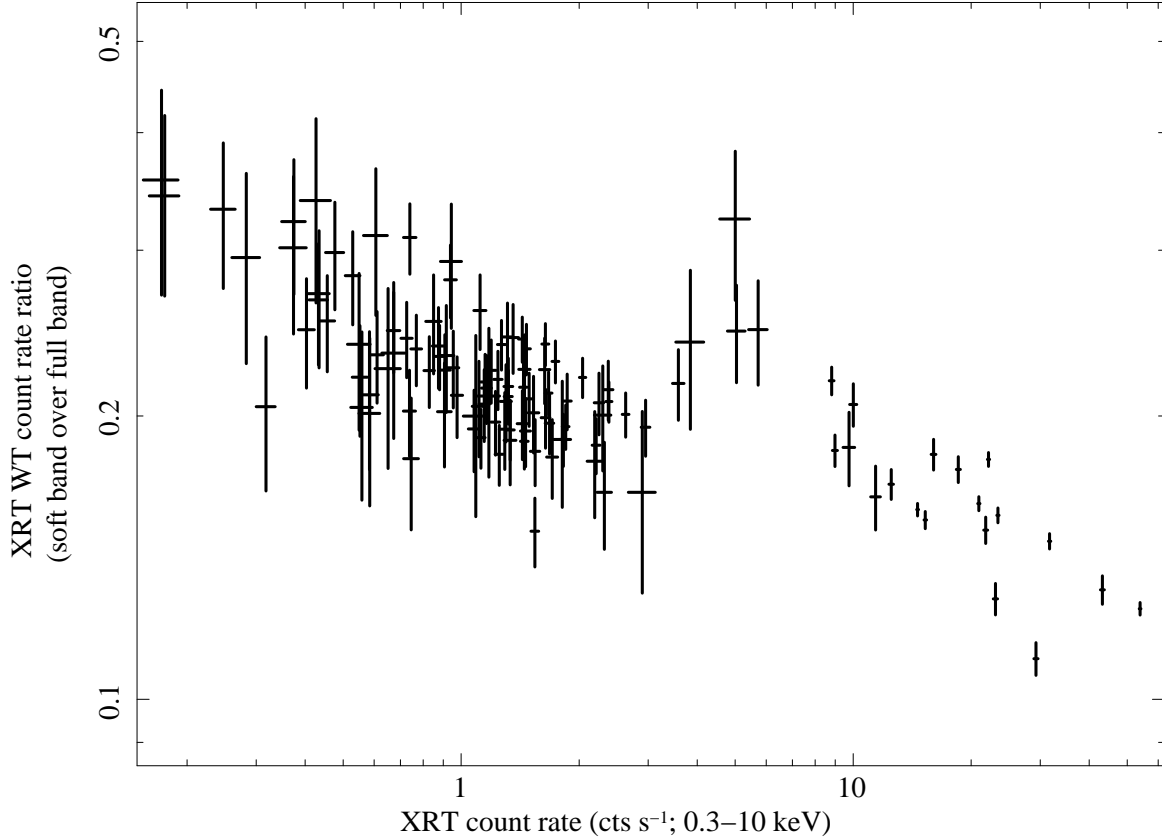
Supplementary Figure 2 | Swift XRT count rate light curve of Sw J1644+57, through 14 April 2011.

Following nearly 3 days of intense flaring with peak count rates of over 80 cts s^{-1} , the source decayed for several days to a count rate of about 0.7 cts s^{-1} , then rose to $\sim 2 \text{ cts s}^{-1}$, where it has remained (with excursions) for over 9 days. From ~ 13 days after the BAT trigger, the light curve can be described by a mean level of $\sim 1 \text{ cts s}^{-1}$, with episodes of dipping that last 1–2 days where the count rate drops to as low as 0.2 cts s^{-1} .

for energy losses incurred by charge traps that have developed on the CCD. These software and calibration files are only available to the XRT team at the time of this analysis, but will be released to the public by the time this paper is published. They are the result of several years of calibration efforts by the XRT team to correct for the effects of radiation damage to the XRT detector after > 6 years in orbit. They provide significant improvements in the spectral resolution and flux calibration compared with earlier versions. We used the latest pre-release spectral redistribution matrices (swxwt0to2s6_20010101v013.arf and swxwt0to2s6_20070901v013.rmf for WT data and swxpc0to12s6_20010101v012.arf and swxpc0to12s6_20070901v012.rmf for PC data).

Intensity-selected spectra We produced XRT spectra in seven intensity ranges for data collected from March 28 until April 7 2011. Events were accumulated with count rates in the following intervals < 0.5 , $0.5 – 1$, $1 – 2.5$, $2.5 – 10$ counts s^{-1} for the PC data, and < 11 , $11 – 35$, > 35 counts s^{-1} for WT data. We corrected the PC data for pile-up by determining the size of an exclusion region at the core of the PSF necessary to get agreement between the wings of the observed PSF and the nominal PSF³¹, and excluding from the analysis all the events that fell within that region.

The spectra were fit with several models. In all cases the absorption consisted of two components, one fixed to the Galactic value ($N_{\text{H}} = 1.7 \times 10^{20} \text{ cm}^{-2}$), and one free at the redshift $z = 0.35$. The following models provided



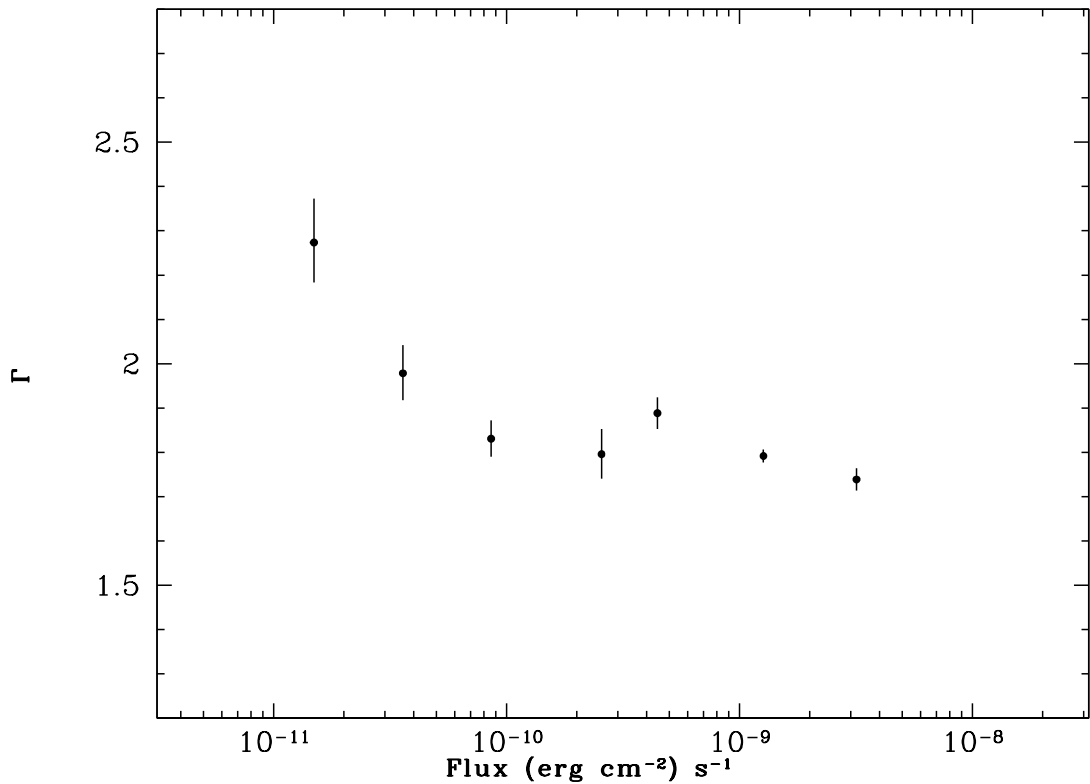
Supplementary Figure 3 | Ratio of XRT count rates in the 0.3–1.3 keV and 0.3–10 keV bands, plotted against the overall XRT count rate. The band ratio is strongly correlated with the overall count rate, demonstrating that the spectrum gets progressively harder as the flux increases. There is a discontinuity around 4 ct/s; data at higher count rates were collected during flares in the first few days of monitoring, whilst data at lower count rates were collected after the XRT observing mode was changed from Auto to WT 14.5 days after the BAT trigger. The trend for harder spectra at higher count rates is seen on both sides of this discontinuity. This figure includes only WT-mode data taken within 23 days of the first BAT trigger. Each data point averages all WT data collected within a single *Swift* orbit. Only data points with uncertainties smaller than 25% are shown.

good fits to the data: *i*) a simple absorbed power-law model (tbabs*zwabs(powerlaw)); *ii*) a log-parabola model (tbabs*zwabs(power2)); *iii*) a broken power-law model (tbabs*zwabs(bknpower)). *iv*) an absorbed power-law model plus a diskblackbody (tbabs*zwabs(powerlaw+diskbb)). The “power2” log-parabola model is defined as:

$$A(E) = E^{(-\alpha + \beta * \log E)} \quad (1)$$

The spectra are comparably well-fit well by either a log-parabola, a broken power-law or power-law plus multi-temperature thermal model. Again, we observe a trend for softer spectra as the source intensity decreases (see Supplementary Figure 4).

Time-selected spectra Spectra were also accumulated from all available XRT data with the aim of obtaining at least 3000 counts per spectrum, unless relevant intensity variations were observed, in which cases more spectra were extracted, to represent the different intensity states. Hence some spectra were also extracted with fewer counts than 3000. We obtained a total of 32 PC spectra and 98 WT spectra, and we fit them with the first three models described



Supplementary Figure 4 | *Swift* XRT intensity-resolved spectral fitting results utilizing an absorbed power-law model. Flux is for the 0.3–10 keV band. The power law slope is strongly correlated with the count rate, confirming the band ratio results shown in Supplementary Figure 3.

above. The simple power-law model is an adequate description of the data, as is the log-parabola (F-test probabilities $\sim 10^{-3}$). We find that the column density is variable in time with no evidence of increased column when the dips occur. The results of the temporally resolved log-parabola model fits are shown in Supplementary Figure 5; in particular, the harder when brighter trend is also observed (the average photon index during the first three days and on the 15th day is 1.78 ± 0.02 and 1.91 ± 0.08 , respectively).

Flux-calibrated XRT light curves The results of the spectral analysis with the log-parabola fits were used to calculate energy correction factors (ECFs) for conversion from the XRT count rate light curve shown in Supplementary Figure 2 to the flux-calibrated light curve presented in Figure 2 of the main Letter. The absorption-corrected fluxes (corresponding to the observed fluxes in Supplementary Figure 5) were used to calculate ECFs corresponding to each time-resolved spectrum. These ECFs were then interpolated to the time of each bin in the count rate light curve of Supplementary Figure 2. The interpolated ECFs were multiplied by the counts in each light curve bin to obtain the absorption-corrected flux light curve.

The flux light curve was used to estimate the total X-ray energy produced by Sw J1644+57. The total measured unabsorbed fluence is $1.24 \times 10^{-4} \text{ erg cm}^{-2}$. Correcting for the live-time fraction, this gives a total unabsorbed fluence for Sw J1644+57 of $7.1 \times 10^{-4} \text{ erg cm}^{-2}$ in the observed 0.3–10.0 keV band. Each flux point in the light curve was also converted to a luminosity at the source, and these were summed to obtain an estimate of the total X-ray energy (corrected for live-time fraction) of $3 \times 10^{53} \text{ erg}$ in the 0.4–13.5 keV rest frame energy band. Mean, median, peak and minimum flux and luminosity values for Sw J1644+57 are given in Supplementary Table 4.

Supplementary Table 4 | X-ray Rest Frame Flux and Luminosity of Sw J1644+57.

Flux Level	Observer frame	Rest frame
	Unabsorbed Flux (0.3–10.0 keV)	Luminosity (0.4–13.5 keV)
Max flux	1.03×10^{-8} erg cm $^{-2}$ s $^{-1}$	4.30×10^{48} erg s $^{-1}$
Mean flux	1.35×10^{-9} erg cm $^{-2}$ s $^{-1}$	5.63×10^{47} erg s $^{-1}$
Median flux	7.07×10^{-10} erg cm $^{-2}$ s $^{-1}$	2.96×10^{47} erg s $^{-1}$
Min flux	3.35×10^{-12} erg cm $^{-2}$ s $^{-1}$	1.40×10^{45} erg s $^{-1}$

XRT spectra for SEDs We also extracted spectra for use in our SED during three epochs representing three intensity states: *i*) strictly simultaneous with the event-mode BAT spectrum; *ii*) a very low state (4.5–5.1 days after the trigger); *iii*) an intermediate state (6.5–9.4 days after the trigger). The XRT data for these states are plotted in Supplementary Figures 11–13.

Simultaneous BAT+XRT spectral fits The results of fitting the BAT+XRT spectral data simultaneously for one of the early flares can be seen in Supplementary Figure 6. We find that for this time period the BAT and XRT spectral fit are consistent, fitting well a broken power-law model. The BAT 15–150 keV spectrum is a continuation of the XRT spectrum, and there is no need for additional spectral breaks or high energy components to fit the BAT spectrum. Unfortunately it is not possible to fit perform simultaneous fits at all epochs, due to source faintness and the limitations of the Survey data collection mode of the BAT during regular observations. The spectral parameters appear to be strongly dependent on the X-ray flux (see Supplementary Figures 3–4). Therefore in order to test whether the BAT spectra were typically consistent with the XRT fits, we fit a broken power-law model to the XRT spectrum at various flux levels, and then extrapolated this model to estimate the expected count rate seen in the BAT energy band. We found that the BAT count rates are highly consistent with the extrapolated XRT spectral fits, suggesting that the consistency seen in the BAT+XRT spectral fit show in Supplementary Figure 6 is true also for later time data.

Observations by other X-ray/γ-ray observatories

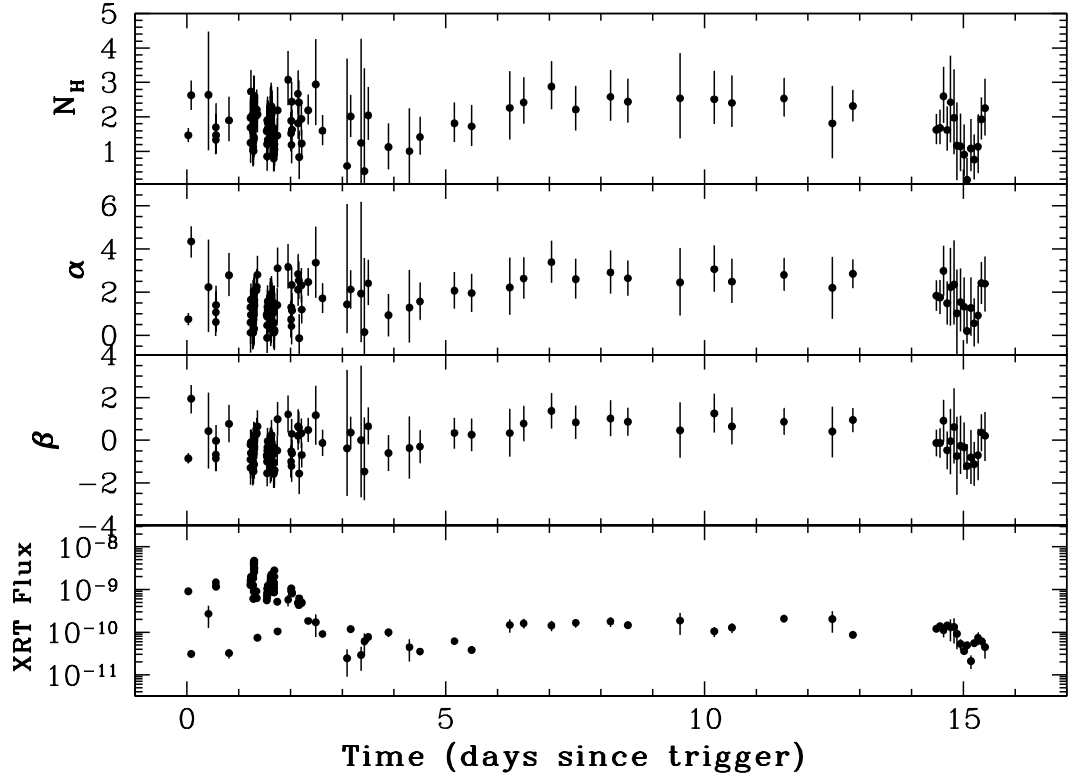
MAXI Following the BAT on-board trigger, the *MAXI*³⁷ team reported that the Gas Slit Camera³⁸ also detected Sw J1644+57³⁹. The source rises to a peak about a day after the first BAT trigger. *MAXI* continued to detect the source for the initial bright flaring part of the outburst. The *MAXI* one-day-averaged light curve for the period before and after the BAT trigger is shown in Supplementary Figure 7.

Fermi In the GeV energy range, no significant γ-ray emission has been seen by the *Fermi* Large Area Telescope (LAT) from the direction of Sw J1644+57. During the period of main activity (28 March to 4 April 2011) *Fermi* LAT observations constrain the average γ-ray flux to $< 2.7 \times 10^{-11}$ erg cm $^{-2}$ s $^{-1}$ (100 MeV–10 GeV, 95% confidence upper limit). During the following week, the equivalent upper limit is 2.9×10^{-11} erg cm $^{-2}$ s $^{-1}$. Daily upper limits during the X-ray outburst vary, but are typically a few times 10^{-10} erg cm $^{-2}$ s $^{-1}$. For the LAT analysis the event class used was “DIFFUSE” and the version of the instrument response functions used was Pass 6, v3 (P6_V3_DIFFUSE).

UV/Optical/NIR observations

Sw J1644+57 has been observed by a large number of ground-based optical and radio telescopes. In general, the heavily extinguished optical counterpart is not clearly detected in optical or UV bands, where the host galaxy dominates the light, but is detected strongly in the near-infrared. Spectroscopic observations identified emission lines at a redshift of 0.354^{40,41}. Here we report details of optical and NIR observations obtained by our team.

R-band Observations *R*-band imaging data were taken using a CCD camera on the Mt. Lemmon Optical Astronomy Observatory (LOAO) 1-m telescope^{42,43} in Arizona, US, and SNUCAM on the Maidanak Observatory 1.5-m

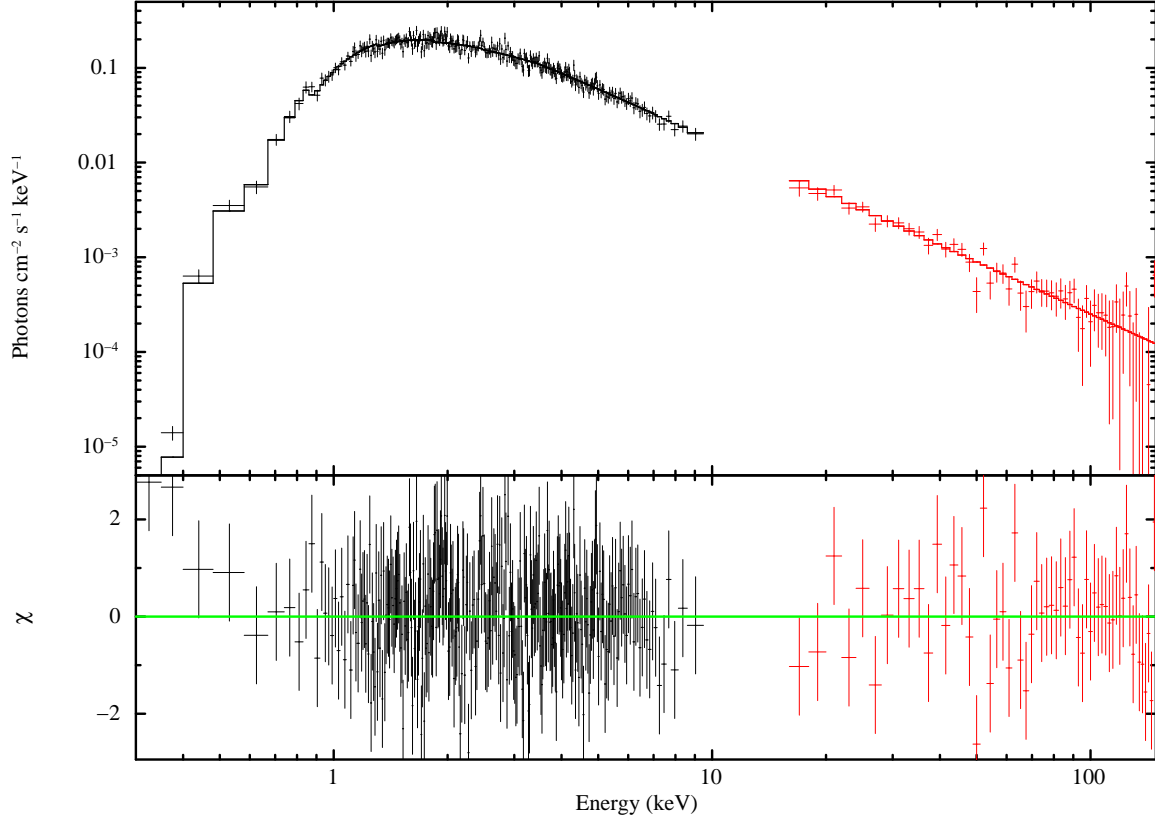


Supplementary Figure 5 | *Swift* XRT time resolved spectral fitting utilizing an absorbed log-parabola model. Parameters α and β for the log-parabola model are as defined in Supplementary Equation 1. N_{H} is the redshift corrected intrinsic absorption in units of 10^{22} cm^{-2} , XRT flux is the observed flux in units of $\text{erg cm}^{-2} \text{ s}^{-1} (0.3\text{--}10 \text{ keV})$.

telescope in Uzbekistan.. The data were taken during the nights of 29 March 2011 to 8 April 2011 at LOAO, and 12 April at Maidanak. A dithered sequence of 300 s – 600 s exposures were taken, resulting in 20 min – 1 hour total integration for each night, which gave 3σ detection limits of $R = 22.4 - 23.9$ mag over a $3''$ diameter aperture. The photometric calibration is based on field calibration performed using four Landolt standard star fields (PG1633+099, SA110, SA107 and PG1657+078) by the Lulin One-meter Telescope operated by National Central University. The summary of our observations and results are in Supplementary Table 5.

BOAO/KASINICS and TNG observations and data analysis We imaged the field of Sw J1644+57 with the Korea Astronomy and Space science Institute (KASI) Near Infrared Camera System (KASINICS⁴⁴) on the 1.8m telescope at the Bohyunsan Optical Astronomy Observatory (BOAO) in Korea, and with the NICS camera⁴⁵ on the Italian 3.6m Telescopio Nazionale Galileo (TNG), located in La Palma, Canary Islands. Near-Infrared J , H and K / K_s -band observations were carried out on nights 30 and 31 March 2011 and 1, 3, 12, 13 and 21 April 2011. All nights were clear, with seeing in the range $1.1'' - 1.3''$. The complete observing log is reported in Supplementary Table 6.

Image reduction was carried out using the jitter pipeline data reduction, part of the ESO-Eclipse package. Astrometry was performed using the 2MASS (<http://www.ipac.caltech.edu/2mass>) catalogue. Aperture photometry was made with the photom tool implemented in the GAIA package and the photometric calibration to the K_s band was done against the 2MASS catalogue. In order to minimize any systematic effect, we performed differential photometry with respect to a selection of local, isolated and unsaturated reference stars visible in the field of view.



Supplementary Figure 6 | *Swift* combined BAT/XRT ‘unfolded’ spectra for Sw J1644+57. The black points are XRT data and the red points are BAT data. The data are from the time interval 19:57:52.0 – 20:04:32.0 UT on 29 March 2011, during one of the bright flares. This figure shows the spectrum incident on the instruments. The solid line is the fitted broken power-law model. The spectra are equally well-fit by a combination of a multi-temperature disk and a power law.

The *Swift* XRT light-curve (Supplementary Figure 2) shows strong variability at essentially any epoch, and hints of an analogous behaviour in the NIR band are seen when considering the whole dataset. In particular, after the maximum NIR flux observed about 2 days after the first *Swift* trigger, global flux decreases are seen in the NIR data (see Supplementary Figure 8). About a week after the trigger the NIR flux seems to have entered a rather stable phase, which is still lasting more than three weeks after the burst. It seems likely that the late-time NIR data are due to the host galaxy contribution.

By means of almost simultaneous z , J , H , K , and L observations (combining our data with those of Levan et al.⁴⁰) in the first days after the *Swift* trigger when the transient was brighter, we can use the SED of the transient to evaluate the presence of substantial rest-frame extinction. Modelling the SED with a power-law in frequency we find that solutions with a rather flat or even increasing spectrum are favored ($\nu \sim 1/3$). The required extinction, assuming a Milky Way extinction curve⁴⁶, is in the range $E_{B-V} \sim 1 - 3$, with a strong covariance with the spectral index. The required extinction is indeed consistent with the observed constancy of the R-band flux. The R-band emission is due to the galaxy only and was already detected before the transient event⁴⁷, while the transient contribution is depressed by local intrinsic absorption well below the host-galaxy brightness.

Historical X-ray/γ-ray Upper Limits

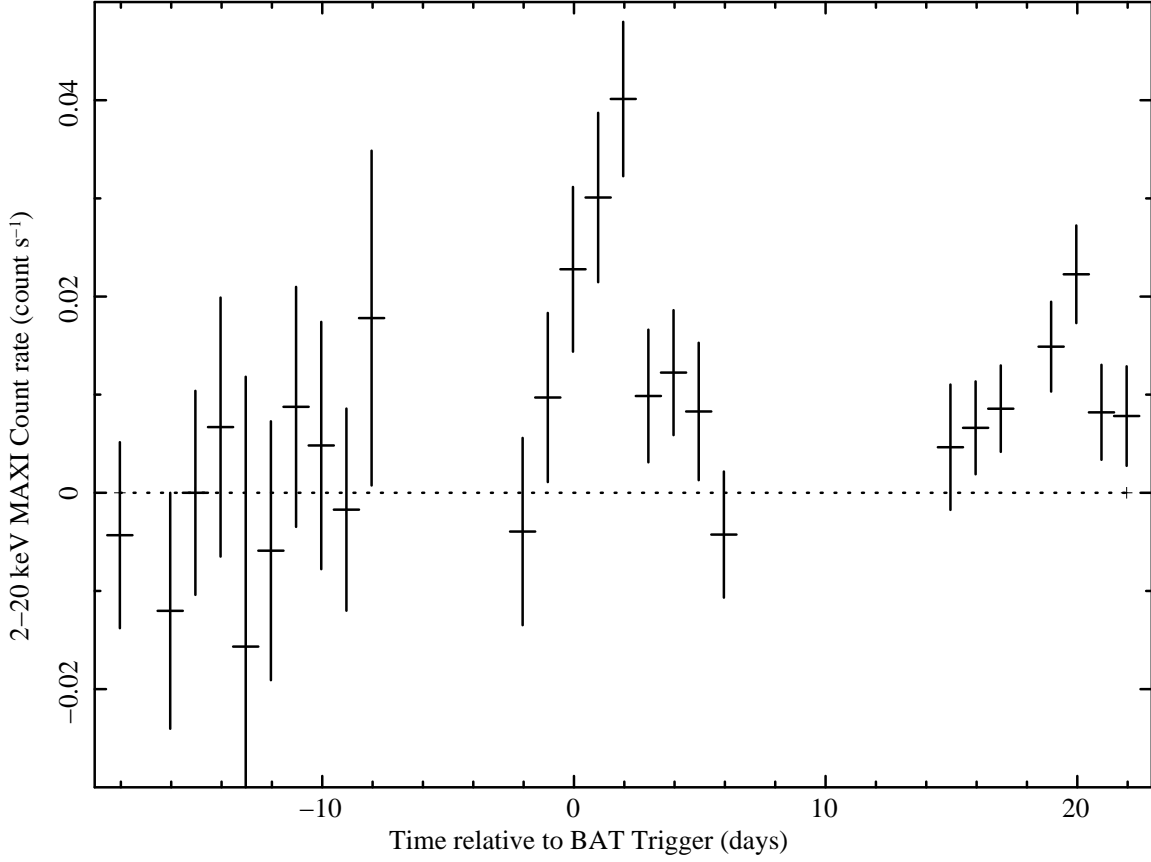
We have examined archival databases from several X-ray and γ -ray instruments that have observed the location of Sw J1644+57, either through wide field surveying or in serendipitous pointings, to search for earlier detections of a

Supplementary Table 5 | Log of R-band observations of Sw J1644+57.

Start(UT)	End(UT)	Time(Mid Time) (UT)	Filter	Exp(s)	Magnitude
LOAO:					
2011-03-29T10:53:45	2011-03-29T10:59:51	2011-03-29T10:56:48	R	300×5	22.45 ± 0.49
2011-03-30T10:50:24	2011-03-30T11:47:47	2011-03-30T11:19:06	R	300×12	22.33 ± 0.22
2011-04-05T11:15:26	2011-04-05T12:02:33	2011-04-05T11:39:00	R	300×6	22.35 ± 0.25
2011-04-06T11:18:05	2011-04-06T12:22:00	2011-04-06T11:50:03	R	300×12	22.20 ± 0.31
2011-04-08T10:09:28	2011-04-08T11:29:07	2011-04-08T10:49:17	R	300×14	22.73 ± 0.26
Maidanak Observatory:					
2011-04-12T22:49:39	2011-04-12T23:10:21	2011-04-12T22:59:59	R	600 × 2	22.49 ± 0.12

Supplementary Table 6 | Near Infrared data taken utilizing the TNG telescope and the BOAO telescope.

Time of obs (UT)	δ_T (days)	Telescope	Inst	Filter	Exp (s)	Magnitude
2011-03-30.650910	2.11081	BOAO	KASINICS	K_s	120×43	16.78 ± 0.07
2011-03-31.23164	2.69558	TNG	NICS	K	20×3×40	16.94 ± 0.04
2011-03-31.636350	3.09625	BOAO	KASINICS	K_s	90×32	17.07 ± 0.08
2011-03-31.67763	3.13753	BOAO	KASINICS	H	60×48	18.44 ± 0.09
2011-04-02.13674	4.59748	TNG	NICS	J	60×1×40	20.10 ± 0.12
2011-04-02.17847	4.63973	TNG	NICS	H	20×3×40	19.12 ± 0.09
2011-04-02.22289	4.68682	TNG	NICS	K	20×3×40	17.77 ± 0.10
2011-04-03.648840	6.10874	BOAO	KASINICS	K_s	60×64	18.09 ± 0.11
2011-04-03.689630	6.14953	BOAO	KASINICS	H	60×96	19.06 ± 0.11
2011-04-13.12765	15.59158	TNG	NICS	K	20×3×20	18.24 ± 0.14
2011-04-13.98145	16.44759	TNG	NICS	K	20×3×40	18.34 ± 0.10
2011-04-21.927812	24.40270	TNG	NICS	K	20×3×30	18.22 ± 0.10



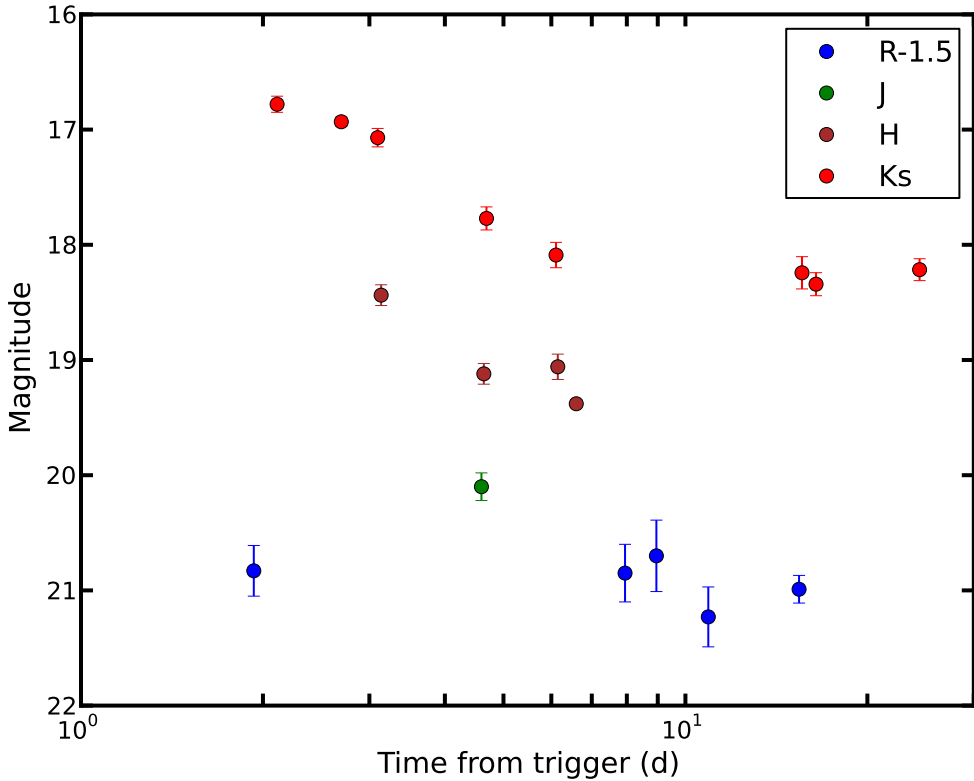
Supplementary Figure 7 | MAXI one-day-averaged light curve covering the \sim 20 days before and after the detection of Sw J1644+57 by BAT.

source from this direction at a variety of wavelengths.

BAT Historical upper limits The BAT instrument monitors about 80% of the sky daily. Examining the BAT Survey data at the location of Sw J1644+57, we find that the hard X-ray source never exceeded the 6σ significance level when it was in the BAT field of view between February 2005 and March 2011 (count rate and flux limits vary with each observation), and was not found in any of the BAT survey studies^{48,49} down to a limiting flux of 10^{-11} erg cm $^{-2}$ s $^{-1}$ (15-150 keV), about two orders of magnitude below the average flux for the first 3 days after the BAT trigger.

The BAT data are also monitored daily for transient events. We searched the entire BAT data set from 12 February 2005 to 28 March 2011, searching for previous detections of Sw J1644+57 on three timescales. The source is not detected on 16-day timescales, with a 3σ upper limit of 0.0011 cts cm $^{-2}$ s $^{-1}$ (about 5 mCrab). On one 1-day timescales, we obtain marginal detections exceeding 3σ on 31 March 2009, 14 September 2009, and 14 March 2011, all at about 0.0036 ± 0.0011 cts cm $^{-2}$ s $^{-1}$; this rate is consistent with the expected rate of false 3σ fluctuations in a search of 1866 independent measurements, and we therefore do not consider these detections to be significant. With the exception of these three days, the 1-day 3σ upper limits vary depending on the total exposure of the source, but are between 0.0010 and 0.0015 cts cm $^{-2}$ s $^{-1}$ for 90% of the observations. On shorter timescales, we can state that the source never exceeded the 6σ significance level on any timescale between 64 s and 1200 s when it was in the BAT field of view (count rate and flux limits vary with each observation) until it triggered the BAT in a 1200 second image trigger on 28 March 2011.

ROSAT Historical Upper Limits Sw J1644+57 was serendipitously observed in a 6.5 ks *ROSAT* PSPC-B obser-



Supplementary Figure 8 | Optical/NIR light curves in the R (blue), J (green), H (brown) and Ks (red) bands of Sw J1644+57. No variability has been detected in the R band while in the NIR a decay trend roughly consistent with X-ray data is visible. Error bars are 1σ .

vation made on 3 April 1992 covering the energy range $0.1 - 2.35$ keV. The source is $\sim 42'$ off axis and is affected by shadowing from one of the PSPC windows support ribs, giving an effective exposure time of 3.3 ks. The 3σ upper limit⁵⁰ for the PSPC count rate is 8.3×10^{-3} cts s $^{-1}$, corresponding to an observed $0.3 - 10$ keV flux limit of $< 2.9 \times 10^{-13}$ erg cm $^{-2}$ s $^{-1}$ (observed) for any of the spectral models that fit the XRT data. We note that no source is detected at even the 1.5σ level. This limit is more than an order of magnitude below the faintest portion of the XRT light curve, and four orders of magnitude below the brightest flares. Upper limits on the flux for different spectral models for Sw J1644+57 are given in Supplementary Table 7.

The *ROSAT* All-Sky Survey also covered this field with a relatively long exposure due to its high ecliptic latitude, collecting 940 s of data between 11 July 1990 and 13 August 1991. These data provide a 3σ PSPC count rate upper limit⁵⁰ of 7.3×10^{-3} cts s $^{-1}$, with a corresponding $0.3 - 10$ keV flux limit of $< 2.5 \times 10^{-13}$ ergs cm $^{-2}$ s $^{-1}$.

XMM-Newton Historical Upper Limits Although there were no pointed observations of the Sw J1644+57 field by *XMM-Newton* prior to the outburst, between 26 August 2001 and 25 March 2011 *XMM-Newton* slewed over this object on one occasion at 01:42:32 UT on 27 July 2005. The EPIC-pn routinely takes data during such slews⁵¹. No detection was made during the 3.9 s exposure made with the medium filter, resulting in a 2σ upper limit of < 0.79 cts s $^{-1}$ (0.2–12 keV), calculated following the Bayesian approach of Kraft, Burrows & Nousek⁵⁰. Unabsorbed 0.2–12 keV flux limits were derived for the following three spectral models: a power law spectrum of photon index $\Gamma = 2.8$ absorbed by a Hydrogen equivalent column density of $N_H = 7.7 \times 10^{21}$ cm $^{-2}$, a broken power law with $\Gamma_1 = 4.98, \Gamma_2 = 2.48, E_{break} = 1.96$ keV, and $N_H = 1.30 \times 10^{22}$ cm $^{-2}$, and a disk blackbody plus power law model with

Supplementary Table 7 | 3σ upper limits based on *ROSAT* data for various spectral models

All fluxes are 3σ upper limits, $\text{erg cm}^{-2} \text{ s}^{-1}$ (0.3–10 keV)

Model	3 April 1992 Pointed Observation		RASS Observation	
	Observed Flux	Unabsorbed Flux	Observed Flux	Unabsorbed Flux
Simple absorbed power law model ($N_{\text{H}} = 7.73 \times 10^{21} \text{ cm}^{-2}$, $\Gamma = 2.80$):				
	$< 2.88 \times 10^{-13}$	$< 1.21 \times 10^{-12}$	$< 2.52 \times 10^{-13}$	$< 1.06 \times 10^{-12}$
Broken power law model ($N_{\text{H}} = 1.30 \times 10^{22} \text{ cm}^{-2}$, $\Gamma_1 = 4.98$, $E_{\text{break}} = 1.96 \text{ keV}$, $\Gamma_2 = 2.48$):				
	$< 2.88 \times 10^{-13}$	$< 1.83 \times 10^{-11}$	$< 2.52 \times 10^{-13}$	$< 1.59 \times 10^{-11}$
Disk black body + power law model ($N_{\text{H}} = 1.24 \times 10^{22} \text{ cm}^{-2}$, $T_{\text{in}} = 175 \text{ eV}$, $\Gamma = 2.40$):				
	$< 2.90 \times 10^{-13}$	$< 4.24 \times 10^{-12}$		

$T_{\text{in}} = 175 \text{ eV}$, $\Gamma = 2.40$, and $N_{\text{H}} = 1.24 \times 10^{22} \text{ cm}^{-2}$; these flux limits were $< 2.9 \times 10^{-12} \text{ erg cm}^{-2} \text{ s}^{-1}$, $< 3.2 \times 10^{-12} \text{ erg cm}^{-2} \text{ s}^{-1}$, and $< 3.2 \times 10^{-12} \text{ erg cm}^{-2} \text{ s}^{-1}$, respectively.

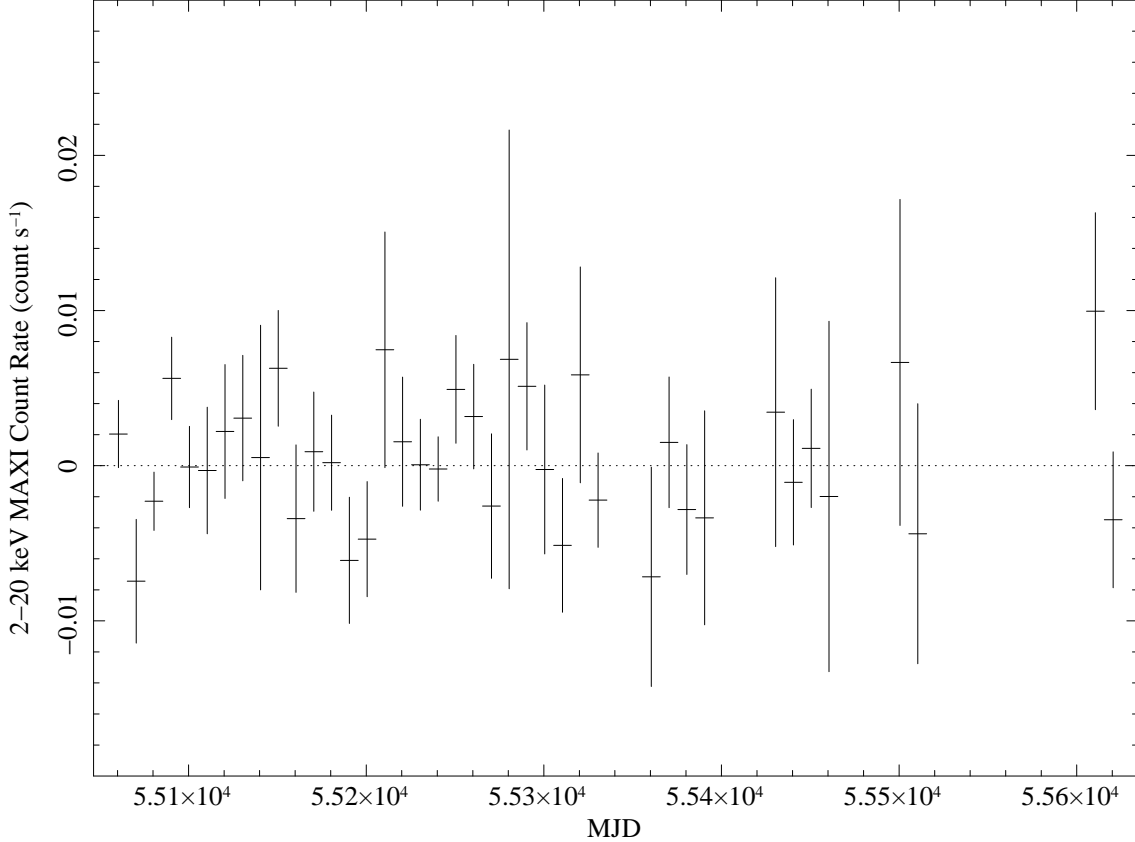
MAXI Historical Upper Limits To investigate whether *MAXI* detected the Sw J1644+57 before the current outburst, we have analysed historical *MAXI* GSC data for the period of 17 August 2009 to 1 March 2011 (see Supplementary Figure 9). No detection of Sw J1644+57 is found in those data, giving a 90% confidence level upper limit of $\sim 1.1 \times 10^{-11} \text{ erg cm}^{-2} \text{ s}^{-1}$ (2-20 keV). In addition to this, utilizing data that has had additional cleaning applied, but covers a narrower time period (between 1 September 2009 and 31 March 2010), we obtain a deeper 90% confidence level upper limit of $2.7 \times 10^{-12} \text{ erg cm}^{-2} \text{ s}^{-1}$ (4-20 keV).

Fermi Historical Upper Limits The analysis of the full 32-month *Fermi*/LAT dataset does not reveal any new source within 3 degrees of the position of the transient. This places 95% confidence upper limits of 1.7×10^{-8} photons $\text{cm}^{-2} \text{ s}^{-1}$ (100 MeV-10 GeV) and 1.5×10^{-10} photons $\text{cm}^{-2} \text{ s}^{-1}$ (1 GeV - 300 GeV) on any persistent prior emission. Given the variable nature of this source, a search for emission was performed on shorter timescales of 2 days and 5 days over the *Fermi* mission lifetime. No significant variation from the mean background level is observed in the light curve (see Supplementary Figure 10).

Supplementary Discussion

Constraints on the Mass of the Central Black Hole

An upper limit to the mass of the central black hole in the galaxy where the transient was observed can be obtained through the black hole mass vs host bulge luminosity relation⁵². Using the measured *B* and *H* magnitudes of the host galaxy from published reports^{53,54} and from our own analysis of *Hubble Space Telescope* WFC3 observations, and taking a luminosity distance of $d_{\text{L}} = 1.88 \text{ Gpc}$, we infer the following luminosities relative to the Sun: $\log(L_{\text{B}}/L_{\odot,\text{B}}) = 9.20$ and $\log(L_{\text{H}}/L_{\odot,\text{H}}) = 9.58$ (the *B*-band luminosity includes a Galactic extinction correction of $A_{\text{B}} = 0.08 \text{ mag}$). These luminosity estimates lead to a black hole mass of $M_{\text{bh}} \approx 2 \times 10^7 \text{ M}_{\odot}$, with a systematic uncertainty of a factor of 2 resulting from the scatter in the empirical relation between the host luminosity and black hole mass. Moreover, this empirical formula relates the luminosity of the *spheroid* of the host galaxy (i.e, its bulge) to



Supplementary Figure 9 | MAXI light curve of Sw J1644+57 for the period August 17 2009 to 1 March 2011. Note that the count rates seen in this light curve are consistent with a non-detection of Sw J1644+57 in this period

the black hole mass. However, the spectrum of the host galaxy shows the spectroscopic signature of star formation⁵⁵, which suggests that it is a spiral. Since the magnitudes we have used refer to the entire galaxy, not just its bulge, the above value is an upper limit to the black hole mass.

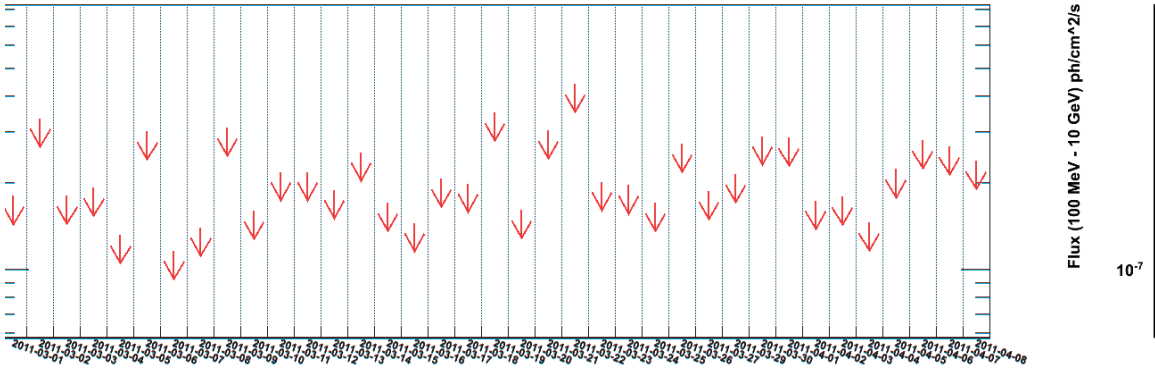
An independent constraint on the black hole mass can be obtained from the minimum X-ray variability time scale, which is observed to be $\delta t_{\min} \sim 100$ s (3 σ value). This time scale constrains the size of the central engine since, for Schwarzschild black hole, the minimum variability time scale is in its rest frame is $\delta t_{\min} \sim r_S/c \sim 100 M_6$ s, where $M_6 = M_{\text{bh}}/10^6 M_{\odot}$. Thus,

$$M_{\text{bh}} \sim 7.4 \times 10^6 \left(\frac{\delta t_{\text{obs}}}{100 \text{ s}} \right) M_{\odot}. \quad (2)$$

Much larger or much smaller masses are unlikely for the following reasons. For larger masses, a variability time scale much shorter than the above constraint was never observed in the X-ray band in other systems containing supermassive black holes (e.g. AGNs)¹. For much smaller masses (e.g. stellar-mass black holes), one would expect to see much shorter variability time scales in the light curves.

Some nearby low-luminosity GRBs with a stellar-mass central engine (e.g. GRB 060218) do have a smooth light curve without a noticeable fast variability component. However, GRB 060218 has only one peak. It would be contrived to have a smaller black hole smear up all the shorter variability time scales but only keep the 100 s time scale. We conclude that the black hole mass is likely $M_{\text{bh}} \sim (10^6 - 2 \times 10^7) M_{\odot}$ ($1 < M_6 < 20$).

¹More rapid TeV variability has been observed in some blazars, which may be attributed to additional local Lorentz boost within a jet (e.g. jet in the jet)⁵⁶.



Supplementary Figure 10 | *Fermi* 95% confidence upper limit light curve of Sw J1644+57 for the period August 17 2009 to 1 March 2011.

Energetics and Their Implications

After the initial flare, the source settled down to an X-ray flux of $F_X \sim 10^{-9}$ erg cm $^{-2}$ s $^{-1}$. The X-ray to γ -ray luminosity is

$$L_{\gamma,X} = 4.2 \times 10^{46} \text{ erg s}^{-1} \left(\frac{F_{\gamma,X}}{10^{-10} \text{ erg cm}^{-2} \text{ s}^{-1}} \right), \quad (3)$$

assuming the above luminosity distance. This luminosity is well above the Eddington limit for a $10^6 M_\odot$ black hole ($L_{\text{Edd}} = 1.3 \times 10^{44} M_6 \text{ erg s}^{-1}$ with $M_{\text{bh}} = 10^6 M_6 M_\odot$), suggesting that the emission originates from a relativistic jet rather than an accretion disk.

The above luminosity, along with the coincidence of the event with the center of the host galaxy⁵⁴, lead us to consider the onset of accretion-powered nuclear activity in the host galaxy. This could be fueled either by the tidal disruption of a star by the central black⁵⁷ hole or by the supply of gas from another source.

To estimate the mass accretion rate and the total mass accreted, let us assume that the accretion rate is $\dot{M} = f \dot{M}_{\text{Edd}}$, where $\dot{M}_{\text{Edd}} = L_{\text{Edd}} / (\eta c^2)$, and η is the usual accretion efficiency. We should allow the factor f to be larger than unity, since the accretion rate, especially for the early phases of the tidal disruption event, can be super-Eddington. Therefore

$$\dot{M} = f \dot{M}_{\text{Edd}} = f \frac{L_{\text{Edd}}}{\eta c^2} = 1.4 \times 10^{23} M_6 \frac{f}{\eta} \text{ g s}^{-1} \quad (4)$$

giving a total mass, accreted until now, of the order

$$M = \Delta t \dot{M} \sim 2 \times 10^{-4} \frac{f}{\eta} \frac{\Delta t}{1 \text{ month}} M_\odot \quad (5)$$

leading to a few per cent of a solar mass if $f/\eta \sim 10^2$. In fact, the measured radiative energy in the 0.4–13.5 keV rest frame band for the first 23.4 days of activity, 3×10^{53} erg, corresponds to $0.016(\eta/0.1)M_\odot$, assuming isotropic emission.

If the source of fuel is the tidal disruption of a star by the black hole, then we expect an initially super-Eddington flare from the accretion of bound debris, followed by a steady decline that traces the rate of return of post-disruption debris, ($\dot{M} \propto (t - t_0)^{-5/3}$)^{58,59,60}. The monotonic decline phase could lag the initial flare by as much as 1–2 months⁶⁰, though the X-ray light curve (Figure 1 in the Letter) suggests that the decline phase may have begun within a few days of the flare onset for Sw J1644+57. Therefore, long-term monitoring of the source in search of this specific rate of decline will be able to test the tidal disruption scenario.

Modelling the Spectral Energy Distribution of the Emerging Jet

Available Data

Radio Observations – The 8.4 GHz flux density was observed on 1 April⁶¹. The 13.5 GHz, 15 GHz and 100 GHz (3 mm) fluxes were also reported in GCN Circulars^{62,63,64}. Although important, these data will not be used to for the modelling of the X-ray and IR emitting region, since the radio emission must come from a larger region, not to be self-absorbed. Additional radio observations and their interpretation are treated by Zauderer et al.⁶⁵.

IR and Optical Observations – In the Supplementary Methods we present the near-infrared observations performed with the TNG and BOAO telescopes. Of these data, we have selected for the modelling those corresponding to the peak of the IR light curve (approximately 2 days after trigger), at the first minimum of the X-ray light curve (~ 4.5 days), and at an intermediate state about a week after the trigger. The large column density derived from the X-ray fitting, of the order of $N_{\text{H}} \sim 10^{22} \text{ cm}^{-2}$, suggests a large value of the extinction, even if the dust to gas ratio is not known. We de-redden our data with a rest frame $A_V = 4.5$, as discussed in the Supplementary Methods, approximately as in Bloom et al.⁶⁶.

X-Ray Observations – We have chosen to show the spectra for the peak (31 hours from trigger), including BAT data, for the minimum after 4.5 days, and for the intermediate persistent flux state that began a few days after the BAT trigger.

γ -ray Observations – We use the upper limit in the *Fermi*/LAT band reported in the Supplementary Methods.

TeV Observations – The *VERITAS* Collaboration⁶⁷ set an upper limit on VHE emission during the early “flaring” period March 29–March 31 and the later “quiescent” period, April 1–April 15. The two upper limits are reported in the SED shown in Supplementary Figure 11–13.

Assumptions and Observational Constraints on the Model

We assume that the spectrum is produced by the synchrotron and inverse Compton (IC) mechanisms. In general, the seed photons for the inverse Compton process can be produced by the synchrotron process itself (Synchrotron Self-Compton, SSC) or can be produced outside the jet (External Compton, EC). A new-born blazar has had no time to build up a broad line region (i.e., to populate the surroundings of the jet with external photons), but some contribution to the EC process can come from photons produced in the accretion disk. The following is a summary of information we have used to guide the development of the model:

- a limit on the size of the X-ray emitting region from the variability timescale, $t_V \sim 100$ s;
- the isotropic luminosity L_{obs} ; at the peak of the flare is $L_{\text{obs}} = 10^{48} L_{\text{syn,48}}$ erg s⁻¹; there is variability by a factor > 100 ;
- some hints on the peak energy: *Fermi* and *VERITAS* did not detect the source;
- the slope of the line connecting the IR to the X-rays is hard, possibly as hard as $\nu^{1/3}$;
- it is the first time we have ever observed a flare of this kind, therefore the phenomenon is relatively rare.
- the upper limit on the black hole mass derived above is $2 \times 10^7 M_{\odot}$ and a mass compatible with the observed variability is $\sim 7 \times 10^6 M_{\odot}$.

For blazar jets, one can find a unique solution for modelling their spectral energy distribution (SED) when the emission is SSC, and when we know the peak frequencies of the synchrotron and Compton spectra, the slopes before and after the peaks, the peak flux levels, and the variability timescale. Here we do not know anything about the Compton component, and we can only guess the peak frequency (and flux) of the synchrotron component. Therefore we need additional assumptions in order to find a reasonable fit.

One possibility is to assume that: (i) the source is magnetically dominated (note that this is *not* the case for blazars, whose jet powers are dominated by the kinetic energy of particles), and (ii) the self Compton flux must be absorbed by the $\gamma\gamma \rightarrow e^\pm$ process. The first assumption comes from the very hard optical to X-ray spectrum, requiring a low energy cut-off in the particle distribution, and thus indicates a particle-starved source, while the second requirement comes from the *Fermi* and *VERITAS* upper limits.

The size – We assume for simplicity a spherical source of radius R at some distance d from the black hole. We define $\mathcal{D} \equiv 1/[\Gamma(1 - \beta \cos \psi_v)]$ as the Doppler factor, where ψ_v is the viewing angle. Note that for blazars one assumes a mono-directional velocity (unlike in GRBs). The size is constrained by:

$$R \leq ct_v \frac{\mathcal{D}}{1+z} \quad (6)$$

Magnetic field – We assume that the bulk of the luminosity is produced by synchrotron radiation. We further assume that the jet is magnetically dominated. This is because of the very hard slope between the optical and the X-rays, implying that there are no low energy electrons in the source. If there were, then they would severely overproduce the optical flux. One possibility is that the electrons are continuously reaccelerated/heated, in such a way that there are no electrons below, say, $\gamma \sim 10^2 - 10^3$. So we need a “thermal bath”, but with relatively few electrons inside. Otherwise the mean energy of the particles will be small. As a consequence, the jet is particle-starved, and the jet power must be carried by the magnetic field. The jet is however capable of producing a lot of radiation: the isotropic luminosity we see is $L_{\text{obs}} \sim 10^{48} \text{ erg s}^{-1}$, but this is beamed. The real power spent by the jet to produce L_{obs} is

$$P_r \sim \frac{L_{\text{obs}}}{\Gamma^2} \quad (7)$$

up to factor of order unity (see e.g. Ghisellini et al. 2010, MNRAS, 402, 497). If the jet is particle-starved, this power must be given by the Poynting flux, and therefore we require:

$$P_B = \pi R^2 \Gamma^2 c \frac{B^2}{8\pi} > \frac{L_{\text{obs}}}{\Gamma^2} \quad (8)$$

Together with Supplementary Equation 6 this gives the limit:

$$B > \frac{1+z}{\Gamma^2 \mathcal{D} t_v} \left(\frac{L_{\text{obs}}}{8c^3} \right)^{1/2} \quad (9)$$

Pair production – Since we are dealing with a compact source, with a large produced synchrotron luminosity, it is conceivable that the self-Compton emission would be relevant. But the upper limits by *Fermi* tell us that the observed γ -ray flux is much less than the synchrotron flux. One way to account for that is pair opacity. We may therefore require that the optical depth for pair production is larger than unity:

$$\tau_{\gamma\gamma} \sim \frac{\sigma_T}{5} \frac{U'_{\text{ssc}}}{m_e c^2} R > 1 \quad (10)$$

where U'_{ssc} is the comoving synchrotron self-Compton radiation energy density, and $U'_{\text{ssc}}/m_e c^2$ is (very approximately!) the number density of photons at threshold, where $\sigma_{\gamma\gamma} \sim \sigma_T/5$. We then have:

$$\frac{\sigma_T}{5} \frac{L'_{\text{ssc}}}{4\pi R^2 c m_e c^2} R = \frac{\sigma_T}{20\pi} \frac{L'_{\text{ssc}}}{L'_{\text{syn}}} \frac{(L_{\text{syn}}/\mathcal{D}^4)}{R m_e c^3} = \frac{\sigma_T}{20\pi} \frac{L'_{\text{ssc}}}{L'_{\text{syn}}} \frac{L_{\text{syn}}(1+z)}{\mathcal{D}^5 c t_v m_e c^3} > 1 \quad (11)$$

Distance from the black hole – If we assume a conical jet of semi-aperture angle $\theta \equiv 0.1\theta_{-1}$ we have

$$d \sim \frac{R}{\theta} < \frac{10 c t_v \mathcal{D}}{\theta_{-1}(1+z)} \quad (12)$$

Since we continue not to detect the source in γ -rays, while the X-rays vary widely, it is likely that we are observing some sort of a standing shock, or (magnetically dominated) internal shocks. The emission cannot be due to a single traveling blob. A single blob would travel rapidly, expand, and die in a short time.

Some numbers – From Supplementary Equation 11 we can set a limit on \mathcal{D} :

$$\mathcal{D} < 11.4 \left(\frac{L_{\text{syn},48}}{t_{v,2}} \frac{L'_{\text{ssc}}}{L'_{\text{syn}}} \right)^{1/5} \quad (13)$$

where $t_v \equiv 10^2 t_{v,2}$ s. Using this limit in Supplementary Equation 9, we derive a lower limit on B :

$$B > 620 \frac{(\mathcal{D}/\Gamma)^3}{L_{\text{syn},48}^{1/10} t_{v,2}^{2/5}} \left(\frac{L'_{\text{syn}}}{L'_{\text{ssc}}} \right)^{3/5} \text{Gauss} \quad (14)$$

The size should be:

$$R < 2.5 \times 10^{13} t_{v,2}^{4/5} L_{\text{ssc},48}^{1/5} \text{cm} \quad (15)$$

The distance from the black hole, in units of the Schwarzschild radius is

$$\frac{d}{R_S} < 833 \frac{t_{v,2}^{4/5} L_{\text{ssc},48}^{1/5}}{\theta_{-1} M_6} \quad (16)$$

Modelling Procedure and Related Considerations

We use the model described in detail in Ghisellini et al.⁶⁸. The emitting region is assumed spherical, of size R_{blob} , moving with a bulk Lorentz factor Γ and located at a distance d from the black hole of mass M . The bolometric luminosity of the accretion disk is L_{disk} .

The particle energy distribution $N(\gamma)$ [cm⁻³] is calculated by solving the continuity equation where particle injection, radiative cooling and pair production (via the $\gamma-\gamma \rightarrow e^\pm$ process) are taken into account. The created pairs contribute to the emission. The injection function $Q(\gamma)$ [cm⁻³ s⁻¹] is assumed to be a smoothly joined broken power-law, with a slope $Q(\gamma) \propto \gamma^{-s_1}$ and γ^{-s_2} below and above a break energy γ_b :

$$Q(\gamma) = Q_0 \frac{(\gamma/\gamma_b)^{-s_1}}{1 + (\gamma/\gamma_b)^{-s_1+s_2}} \quad (17)$$

In the specific application here, we assumed that electrons below a given γ_0 simply disappear.

The total power injected into the source in the form of relativistic electrons is $P'_i = m_e c^2 V \int Q(\gamma) \gamma d\gamma$, where $V = (4\pi/3)R_{\text{blob}}^3$ is the volume of the emitting region.

The injection process lasts for a light crossing time R_{blob}/c , and we calculate $N(\gamma)$ at this time. This assumption comes from the fact that even if injection lasted longer, adiabatic losses caused by the expansion of the source (which is travelling while emitting) and the corresponding decrease of the magnetic field would make the observed flux decrease. Therefore the computed spectra correspond to the maximum of a flaring episode.

Above and below the inner parts of the accretion disk there is an X-ray emitting corona of luminosity L_X (it is fixed at a level of 30% of L_d). Its spectrum is a power law of energy index α_X ending with a exponential cutoff at $E_c = 150 \text{ keV}$. The specific energy density (i.e., as a function of frequency) of the disk and the corona are calculated in the comoving frame of the emitting blob, and used to properly calculate the resulting external inverse Compton spectrum. The internally produced synchrotron emission is used to calculate the synchrotron self Compton (SSC) flux. In this specific case we assume no Broad Line Region; the disk and the coronal radiation are negligible if the emitting region is at a large distance from the disk, but they become important producers of seed photons if the distance d of the emitting blob from the disk is of the same order of (or less than) the outer radius of the disk.

Results and Discussion

Supplementary Table 8 lists three sets of parameters adopted to generate three different models. In Supplementary Figures 11–13 we show the models resulting from these input parameters. Supplementary Table 9 lists the power

carried by the jet in the form of radiation (P_r), magnetic field (P_B), emitting electrons (P_e , no cold electron component is assumed) and cold protons (P_p , assuming one proton per emitting electron). All the powers are calculated as

$$P_i = \pi R_{\text{blob}}^2 \Gamma^2 \beta c U'_i \quad (18)$$

where U'_i is the energy density of the i component, as measured in the comoving frame. We note the following regarding Supplementary Table 9:

- The power carried in the form of radiation, $P_r = \pi R_{\text{blob}}^2 \Gamma^2 \beta c U'_{\text{rad}}$, can be rewritten as [using $U'_{\text{rad}} = L' / (4\pi R_{\text{blob}}^2 c)$]:

$$P_r = L' \frac{\Gamma^2}{4} = L \frac{\Gamma^2}{4\mathcal{D}^4} \sim L \frac{1}{4\mathcal{D}^2} \quad (19)$$

where L is the total observed non-thermal luminosity (L' is in the comoving frame) and U'_{rad} is the radiation energy density produced by the jet (i.e. excluding the external components). The last equality assumes $\psi_v \sim 1/\Gamma$.

- When calculating P_e (the jet power in bulk motion of emitting electrons) we include their average energy, i.e. $U'_e = n_e \langle \gamma \rangle m_e c^2$.
- For P_p (the jet power in bulk motion of cold protons) we have assumed that there is one proton per emitting electron, i.e. electron-positron pairs are negligible. This is unimportant for the models shown in Supplementary Figure 11 and 12, since in these cases the mean energy of the electrons is comparable to the rest mass of protons ($\langle \gamma \rangle m_e \approx m_p$). However, for the model shown in Supplementary Figure 13, P_p is the dominant form of power.
- P_B is derived using the magnetic field found from the model fitting.

In summary, we have studied the extreme cases of a jet whose power is largely dominated by the magnetic field (Models 1,2; Supplementary Figures 11 and 12) or by the kinetic energy of the matter (Model 3; Supplementary Figure 13).

A magnetic field-dominated jet

Our rationale for this model is that since the accretion can be super-Eddington, the density of the accreting matter is large and can sustain a very large B -field, which launches the jet. In the dissipation region, the B -field is still large, possibly because it has not completed the acceleration of the matter. Dissipation can occur at the expense of the magnetic field, through reconnection.

Models shown in Supplementary Figures 11 and 12 rely on the SSC process (the magnetic energy density dominates over the radiation energy density of external seed photons), but adopt different black hole masses: $10^6 M_\odot$ and $10^7 M_\odot$, respectively. In the first model the disk luminosity is kept constant at the Eddington value, even if the jet luminosity and its power change, while in the second model we have assumed that the jet luminosity is tracking a fastly varying accretion luminosity. In this case, for the high state we have assumed a super-Eddington luminosity, and nearly Eddington for the low state. As can be seen, the disk luminosity can barely contribute to the soft X-ray flux.

The dotted orange line in both models shows the flux emitted from a much larger region of the jet, producing the radio flux.

A matter dominated jet

For this model we assume that even if, at the start, the jet is dominated by the magnetic field, nevertheless the Poynting flux is able to accelerate the jet to its final Γ before the dissipation region. The jet is then dominated by the kinetic energy of matter, therefore dissipation is at the expense of the latter, as in all other blazars. The source of the seed photons is an accretion disk with an outer radius of $\gtrsim 300$ Schwarzschild radii (it is $500 R_S$ for the model shown in Supplementary Figure 13). This model is similar to models used for blazars, but with a particle energy distribution that does not extend up to such large energies (i.e. $\gamma_{\text{max}} \sim 80-100$), with most of the electrons at low energies. Therefore in

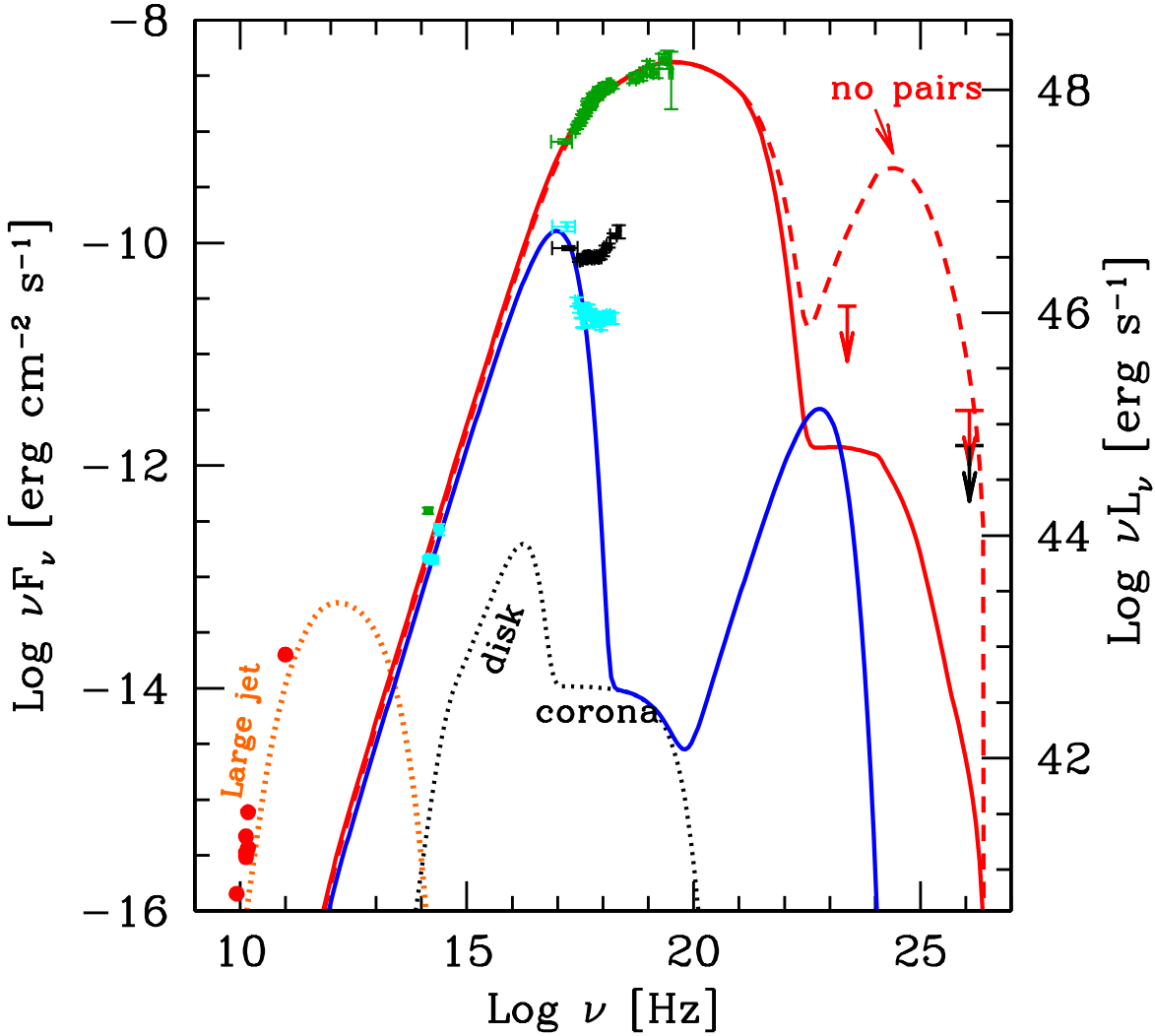
Supplementary Table 8 | Input parameters used to model the SED. Col. [1]: state; Col. [2]: size of the emitting region, in units of 10^{15} cm; Col. [3]: black hole mass in solar masses; Col. [4]: Disk luminosity in units of 10^{45} erg s $^{-1}$ and (L_d/L_{Edd}) ; Col. [5]: power injected in the blob calculated in the comoving frame, in units of 10^{45} erg s $^{-1}$; Col. [6]: magnetic field in Gauss; Col. [7]: bulk Lorentz factor; Col. [8]: viewing angle in degrees; Col. [9]: Doppler factor; Col. [10], [11] and [12]: minimum, break and maximum random Lorentz factors of the injected electrons; Col. [13] and [14]: slopes of the injected electron distribution $[Q(\gamma)]$ below and above γ_b ; Col. [15] $t_v \equiv R_{\text{blob}}(1+z)/(c\mathcal{D})$. The disk has an X-ray corona of luminosity $L_X = 0.3L_d$. The spectral shape of the corona is assumed to be $\propto v^{-1} \exp(-hv/150 \text{ keV})$ for the models in Supplementary Figure 11 and Supplementary Figure 13, while it is $\propto v^{-0.7} \exp(-hv/150 \text{ keV})$ in Supplementary Figure 12.

State [1]	R_{blob} [2]	M [3]	$L_d (L_d/L_E)$ [4]	P'_i [5]	B [6]	Γ [7]	ψ_v [8]	\mathcal{D} [9]	γ_0 [10]	γ_b [11]	γ_{max} [12]	s_1 [13]	s_2 [14]	t_v [15]
Model 1: Supplementary Figure 11														
High	0.03	1e6	0.13 (1)	0.15	3642	10	3	15.7	700	7e3	1e5	0.	2.2	86 s
Low	0.03	1e6	0.13 (1)	1.2e-2	3642	10	3	15.7	600	800	900	0	4.2	86 s
Large	27	1e6	0.13 (1)	1e-6	2.1	19	2	26.3	40	200	400	2.5	3.5	12.8 h
Model 2: Supplementary Figure 12														
High	0.048	1e7	45 (30)	0.048	6014	12	2	20.4	500	9e3	4e4	0	2.4	106 s
Low	0.048	1e7	0.6 (0.4)	2.7e-3	694	12	2	20.4	1e3	1e3	2.5e3	0	2.8	106 s
Large	18	1e7	1.3 (1)	2e-6	2.1	17	2	25.1	10	100	300	0	2.0	8.9 h
Model 3: Supplementary Figure 13														
High	0.036	1e7	1.3 (1)	0.18	60	13	2	21.5	1	60	80	2.5	3	75 s
Low	0.036	1e7	1.3 (1)	0.06	60	5	2	9.6	1	1	100	8	8	210 s

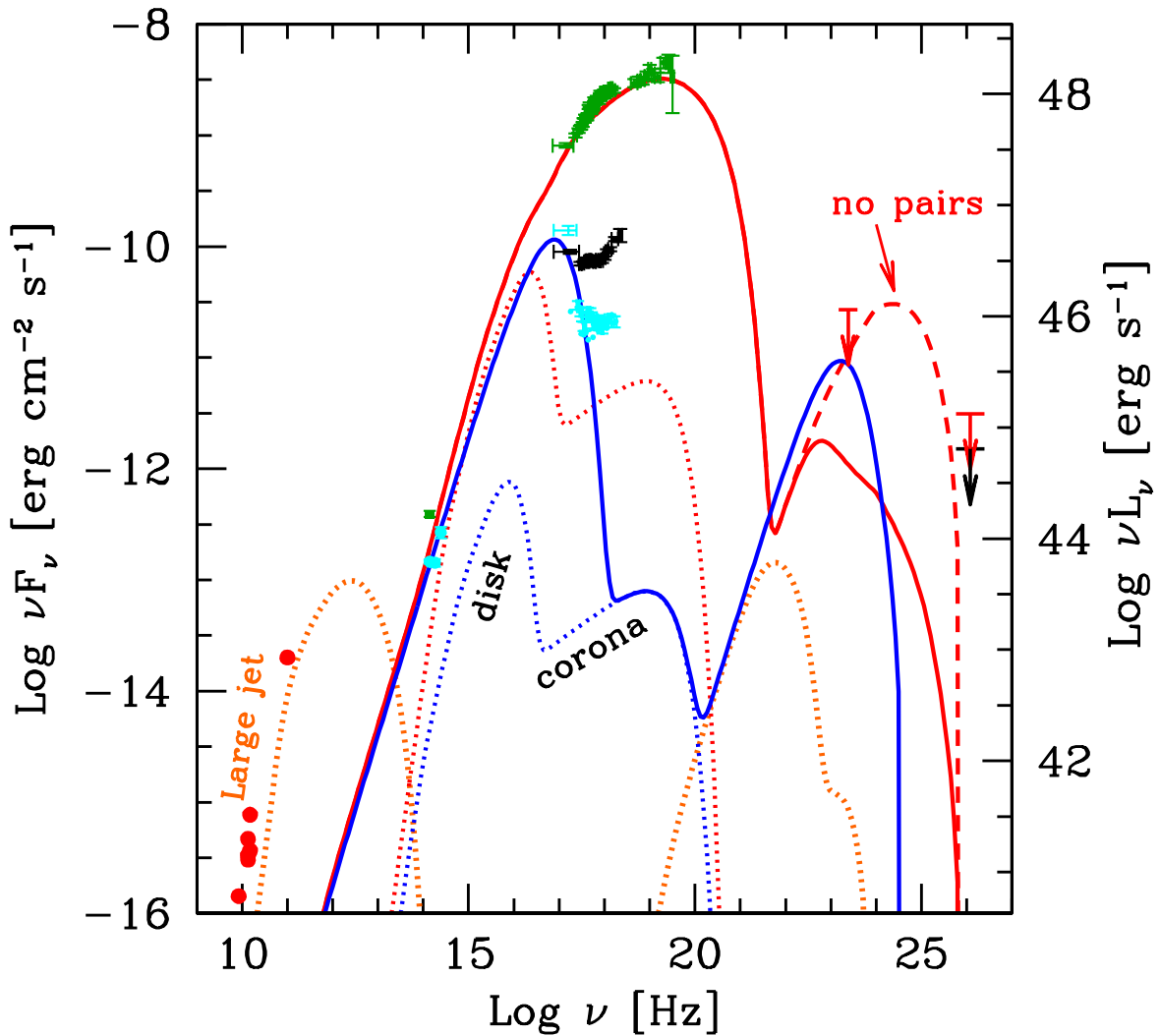
in this case we have a sort of bulk-Compton process, in which relatively cold electrons scatter the seed photons coming from the outer radius of the disk. This model is similar to the one presented by Bloom et al.⁶⁶, but in our case the IR and X-ray photons are produced in the same region. The large L_X/L_{IR} ratio is due to the large ratio between the energy densities of the external radiation and the magnetic field. This requires a small magnetic field, and therefore a matter-dominated jet.

Supplementary Table 9 | Jet power in the form of radiation, Poynting flux, bulk motion of electrons and protons (assuming one proton per emitting electron).

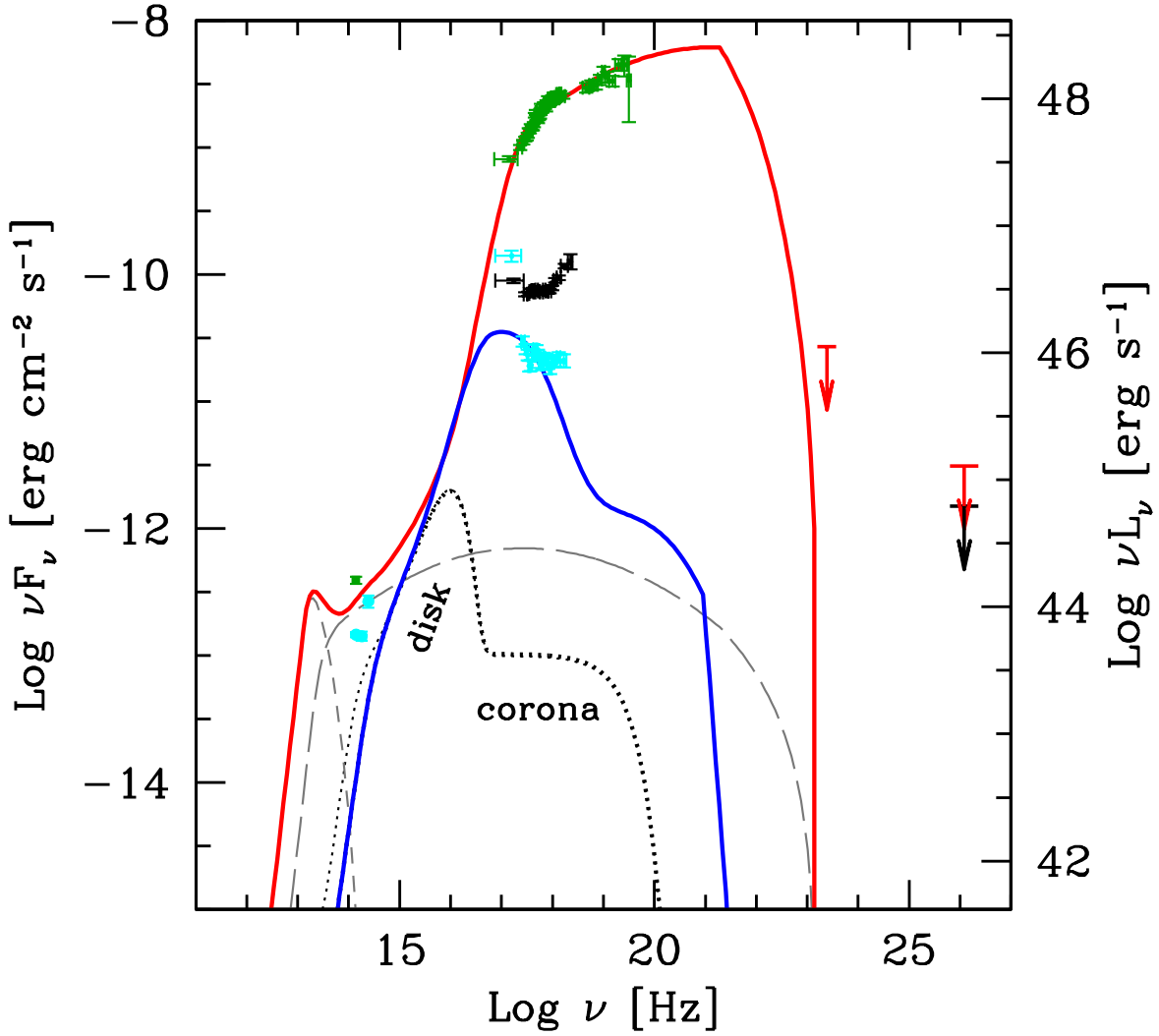
State	$\log P_r$	$\log P_B$	$\log P_e$	$\log P_p$	$L_{0.3-10}/L_{tot}$	L_{15-150}/L_{tot}
Model 1: Supplementary Figure 11						
High	46.12	45.65	41.07	41.05	0.216	0.318
Low	44.33	45.65	40.13	40.55	0.630	1.20e-6
Large	40.82	45.65	41.02	42.43	—	—
Model 2: Supplementary Figure 12						
High	45.78	46.65	40.24	40.34	0.218	0.354
Low	44.03	44.78	40.77	40.95	0.512	8.5e-7
Large	41.30	45.17	41.31	42.71	—	—
Model 3: Supplementary Figure 13						
High	46.14	42.47	44.71	47.74	0.098	0.175
Low	44.17	41.64	43.98	47.19	0.695	0.038



Supplementary Figure 11 | Spectral Energy Distribution for Sw J1644+57. The green data points show the transient brightness in the near-infrared (NIR) K_s band 48 hours after the trigger, while the cyan points show the J , H , and K_s band fluxes 4.5 days after trigger. The NIR flux has been dereddened with $A_V = 4.5$. In the X-ray band we show the spectrum at the peak of the bright flares (31 hours after BAT trigger; XRT and BAT) and in the low flux state (~ 4.5 days after, XRT only), together with the spectrum in the intermediate persistent flux state that began a week after the BAT trigger (time integrated between day 6.5 and 9.5 from trigger, XRT only). The X-ray data have been corrected for absorption with a constant $N_H = 2 \times 10^{22} \text{ cm}^{-2}$. Upper limits from the *Fermi* LAT at $2 \times 10^{23} \text{ Hz}$ and from *VERITAS* at 10^{26} Hz ⁶⁷ are also shown. The red curve shows the model discussed in the text, which is a blazar jet model⁶⁸ fit to our SED. The dominant emission mechanism is synchrotron radiation peaking in the X-ray band. On the low frequency side, the hard slope between the NIR and X-ray bands requires suppression of low-energy electrons, which would otherwise overproduce the NIR flux. On the high frequency side, the LAT and *VERITAS* upper limits require that the self-Compton component is suppressed by γ - γ pair production, without which the model would follow the dashed curve and would significantly overproduce the GeV and TeV emission. The model includes a disk/corona component from the accretion disk (black dotted curve), but the flux is dominated at all frequencies by the synchrotron component from the jet. The blue curve shows the corresponding model in the low X-ray flux state. The kink in the X-ray spectrum suggests a possible additional component may be required; it would have to be very narrow, and its origin is unclear. The radio fluxes come from a larger region of the jet (orange dotted line). See Supplementary Table 8 and Supplementary Table 9 for the model parameters of this fit.



Supplementary Figure 12 | Data as in Supplementary Figure 11. Here the model is similar to that shown in Supplementary Figure 11, but the black hole mass is larger ($M_{\text{bh}} = 10^7 M_{\odot}$), and the jet luminosity is assumed to approximately track a changing disk luminosity, from $30 \times$ Eddington in the high state to $0.6 \times$ Eddington in the low state (dotted lines). The basic features of the jet are similar to the previous case, but the Poynting flux is not constant, instead it tracks \dot{M} .



Supplementary Figure 13 | Data as in Supplementary Figure 11. In this model the NIR flux is synchrotron radiation, and the X-rays are produced by the external Compton. The model assumes a matter dominated jet whose dissipating region is very close to the accretion disk (i.e. $120 R_S$, the black hole mass is assumed to be $10^7 M_\odot$). The disk itself is assumed to extend out to $\sim 500 R_S$. In this case the external part of the disk produces IR photons that can be efficiently scattered by the relativistic electrons in the jet. In order to avoid overproducing the NIR, the magnetic field is small, and the jet must be matter-dominated. The high state (red line) and the low state (blue line) differ in the amount of injected power in relativistic electrons and in the bulk Lorentz factor. The short-dashed gray line is the synchrotron flux in the high state, while the long-dashed line is the corresponding SSC component.

References

25. Gehrels, N. *et al.* The Swift Gamma-Ray Burst Mission. *Ap. J.* **611**, 1005–1020 (2004).
26. Barthelmy, S. D. *et al.* The Burst Alert Telescope (BAT) on the SWIFT Midex Mission. *Space Sci. Reviews* **120**, 143–164 (2005). [arXiv:astro-ph/0507410](https://arxiv.org/abs/astro-ph/0507410).
27. Cummings, J. R. *et al.* GRB 110328A: Swift detection of a burst. *GRB Coordinates Network, Circular Service* **11823** (2011).
28. Sakamoto, T. *et al.* GRB 110328A / Swift J164449.3+573451: BAT refined analysis. *GRB Coordinates Network, Circular Service* **11842** (2011).
29. Barthelmy, S. D. *et al.* GRB 110328A: a second trigger, probably a hard X-ray transient (Swift J164449.3+573451). *GRB Coordinates Network, Circular Service* **11824** (2011).
30. Burrows, D. N. *et al.* The Swift X-Ray Telescope. *Space Sci. Reviews* **120**, 165–195 (2005). [arXiv:astro-ph/0508071](https://arxiv.org/abs/astro-ph/0508071).
31. Vaughan, S. *et al.* Swift Observations of the X-Ray-Bright GRB 050315. *Ap. J.* **638**, 920–929 (2006).
32. Evans, P. A. *et al.* Methods and results of an automatic analysis of a complete sample of Swift-XRT observations of GRBs. *MNRAS* **397**, 1177–1201 (2009). 0812.3662.
33. Roming, P. W. A. *et al.* The Swift Ultra-Violet/Optical Telescope. *Space Sci. Reviews* **120**, 95–142 (2005). [arXiv:astro-ph/0507413](https://arxiv.org/abs/astro-ph/0507413).
34. Poole, T. S. *et al.* Photometric calibration of the Swift ultraviolet/optical telescope. *MNRAS* **383**, 627–645 (2008).
35. Schlegel, D. J., Finkbeiner, D. P. & Davis, M. Maps of Dust Infrared Emission for Use in Estimation of Reddening and Cosmic Microwave Background Radiation Foregrounds. *Ap. J.* **500**, 525–+ (1998).
36. Israel, G. L. & Stella, L. A New Technique for the Detection of Periodic Signals in “Colored” Power Spectra. *Ap. J.* **468**, 369 (1996).
37. Matsuoka, M. *et al.* The MAXI Mission on the ISS: Science and Instruments for Monitoring All-Sky X-Ray Images. *PASJ* **61**, 999– (2009). 0906.0631.
38. Mihara, T. *et al.* Gas Slit Camera (GSC) onboard MAXI on ISS. *PASJ*, in press (2011). 1103.4224.
39. Kimura, M. *et al.* MAXI/GSC observation of Swift J164449.3+573451. *The Astronomer’s Telegram* **3244** (2011).
40. Levan, A. J., Tanvir, N. R., Wiersema, K. & Perley, D. GRB 110328A: Gemini spectroscopic observations. *GRB Coordinates Network, Circular Service* **11833** (2011).
41. Thoene, C. C. *et al.* GRB 110328A / Swift J164449.3+573451: optical spectroscopy from GTC. *GRB Coordinates Network, Circular Service* **11834** (2011).
42. Han, W. *et al.* Development of a 1-m Robotic Telescope System. *PASJ* **57**, 821–826 (2005).
43. Lee, I., Im, M. & Urata, Y. First Korean Observations of Gamma-Ray Burst Afterglows at Mt. Lemmon Optical Astronomy Observatory (LOAO). *Journal of Korean Astronomical Society* **43**, 95–104 (2010).
44. Moon, B. *et al.* KASINICS: Near Infrared Camera System for the BOAO 1.8m Telescope. *PASJ* **60**, 849– (2008).
45. Baffa, C. *et al.* NICS: The TNG Near Infrared Camera Spectrometer. *Astron. and Astrophys.* **378**, 722–728 (2001). [arXiv:astro-ph/0109201](https://arxiv.org/abs/astro-ph/0109201).
46. Pei, Y. C. Interstellar dust from the Milky Way to the Magellanic Clouds. *Ap. J.* **395**, 130–139 (1992).

47. Cenko, S. B., Nugent, P. E., Fox, D. B., Ofek, E. O. & Kasliwal, M. M. GRB 110328A / Swift J164449.3+573451: PTF Quiescent Optical Counterpart. *GRB Coordinates Network, Circular Service* **11827** (2011).

48. Tueller, J. *et al.* The 22 Month Swift-BAT All-Sky Hard X-ray Survey. *Ap. J. Sup.* **186**, 378–405 (2010). 0903.3037.

49. Cusumano, G. *et al.* The Palermo Swift-BAT hard X-ray catalogue. III. Results after 54 months of sky survey. *Astron. and Astrophys.* **524**, A64+ (2010). 1009.0522.

50. Kraft, R. P., Burrows, D. N. & Nousek, J. A. Determination of confidence limits for experiments with low numbers of counts. *Ap. J.* **374**, 344–355 (1991).

51. Saxton, R. D. *et al.* The first XMM-Newton slew survey catalogue: XMMSL1. *Astron. and Astrophys.* **480**, 611–622 (2008). 0801.3732.

52. Marconi, A. & Hunt, L. K. The Relation between Black Hole Mass, Bulge Mass, and Near-Infrared Luminosity. *Ap. J. (Letters)* **589**, L21–L24 (2003). arXiv:astro-ph/0304274.

53. Leloudas, G. *et al.* GRB 110328A / Swift J164449.3+573451: NOT optical observations. *GRB Coordinates Network, Circular Service* **11830** (2011).

54. Fruchter, A. *et al.* GRB 110328A / Swift J164449.3+573451, HST Observations. *GRB Coordinates Network, Circular Service* **11881** (2011).

55. Cenko, S. B. *et al.* GRB 110328A / Swift J164449.3+573451: Keck/DEIMOS Optical Spectroscopy. *GRB Coordinates Network, Circular Service* **11874** (2011).

56. Giannios, D., Uzdensky, D. A. & Begelman, M. C. Fast TeV variability in blazars: jets in a jet. *MNRAS* **395**, L29–L33 (2009). 0901.1877.

57. Rees, M. J. Tidal disruption of stars by black holes of 10 to the 6th-10 to the 8th solar masses in nearby galaxies. *Nature* **333**, 523–528 (1988).

58. Phinney, E. S. Manifestations of a Massive Black Hole in the Galactic Center. In M. Morris (ed.) *The Center of the Galaxy*, vol. 136 of *IAU Symposium*, 543–+ (1989).

59. Evans, C. R. & Kochanek, C. S. The tidal disruption of a star by a massive black hole. *Ap. J. (Letters)* **346**, L13–L16 (1989).

60. Lodato, G., King, A. R. & Pringle, J. E. Stellar disruption by a supermassive black hole: is the light curve really proportional to $t^{-5/3}$? *MNRAS* **392**, 332–340 (2009). 0810.1288.

61. Bower, G., Bloom, J. S. & Cenko, B. Upper Limit on Radio Polarization for GRB 110328A / Swift J164449.3+573451. *The Astronomer's Telegram* **3278**, 1–+ (2011).

62. Pooley, G. GRB 110328A / Swift J164449.3+573451. *GRB Coordinates Network, Circular Service* **11849** (2011).

63. Castro-Tirado, A. J. *et al.* GRB 110328A / Swift J164449.3+573451: millimeter detection at PdBI. *GRB Coordinates Network, Circular Service* **11880** (2011).

64. Mooley, K. *et al.* GRB 110328A / Swift J164449.3+573451: Followup at 15 GHz. *The Astronomer's Telegram* **3252**, 1 (2011).

65. Zauderer, A. *et al.* The Birth of a Relativistic Outflow in the Unusual γ -ray Transient Swift J164449.3+573451. *Nature*, submitted (2011).

66. Bloom, J. S. *et al.* A relativistic jetted outburst from a massive black hole fed by a tidally disrupted star. *ArXiv e-prints* (2011). 1104.3257.

67. Aliu, E. *et al.* The VERITAS Collaboration. *in prep.* (2011).

68. Ghisellini, G. & Tavecchio, F. Canonical high-power blazars. *MNRAS* **397**, 985–1002 (2009). 0902.0793.